

# A Comprehensive Physical-Based Sensitivity Analysis of the Electrochemical Impedance Response of Lithium-Ion Batteries

Claudio Rabissi, Alessandro Innocenti,\* Gabriele Sordi, and Andrea Casalegno

The electrochemical impedance spectroscopy (EIS) characterization technique, although widely adopted in electrochemistry for understanding operational issues and degradation, has a less consolidated physical interpretation in lithium-ion batteries (LIBs), often relying on circuital methods. Herein, the Doyle–Fuller–Newman model is adapted and experimentally validated for the physical simulation of electrochemical impedance; then, it is applied in a comprehensive one-factor-at-time sensitivity analysis on an impedance spectrum from 4 kHz to 0.005 Hz; 28 physical parameters, which represent the kinetic, resistive, diffusive, and geometric characteristics of the battery, are varied within broad literature-based ranges of values, for each of the 20 analyzed battery states, characterized by different state-of-charge and temperature values. The results show a miscellaneous sensitivity of parameters on impedance spectra, which ranges from highly sensitive to negligible, often resulting in a strong dependence on operating conditions and impedance frequency. Such results consolidate the understanding of LIB electrochemical impedance and demonstrate that 40% of the parameters, 12 out of 28, can be considered poorly sensitive or insensitive parameters; therefore, fitting the experimental EIS data, their value can be assumed from the literature without significantly losing accuracy.

## 1. Introduction

The lithium-ion battery (LIB) technology evolved in about 20 years from its first appearance as a commercial product to becoming the undisputed ruler of portable power storage in portable electronics, recently becoming the driver of the much-anticipated electric transition of the transportation sector. High energy and power density, coupled with low self-discharge, satisfying lifetime, and a flexible power-to-energy ratio, are the main enablers for its technological success.<sup>[1–3]</sup> However, cost, performance degradation, safety issues, and environmental sustainability of the whole value chain are serious issues still to be properly addressed to aim for a further improvement of the technology.<sup>[4–6]</sup>

Despite the widespread adoption of LIBs, the understanding of the many mechanisms determining performance and degradation, strongly operation-dependent, reciprocally correlated, and nonlinear in time,<sup>[7,8]</sup> is still less consolidated than in relatively younger


electrochemical technologies. Being the LIB a closed system where all the components and reactants are inaccessible, nondestructive characterization and diagnostics are intrinsically limited in terms of gatherable information, especially in commercial systems, often subjected to industrial secrets. Usually, LIB characterization is limited to the analysis of charge and discharge curve and/or of the pulse-relaxation behavior, where the degrees of freedom are limited to environmental condition, protocol C-rate, and average state-of-charge (SOC) of the battery.<sup>[9–11]</sup> However, such measurements are limited in terms of poor insights from a diagnostic point-of-view, especially if used singularly, resulting in the inability of distinguishing many phenomena interplaying during battery operation.<sup>[12]</sup>

Other than the mentioned tests, the electrochemical impedance spectroscopy (EIS) is regarded as a powerful technique to obtain insights into battery operation and degradation.<sup>[12–15]</sup> Because of its ability to separate mechanisms based on their characteristic timescale, such technique can identify phenomena ranging from internal resistance to charge transfer reactions and mass diffusion. Despite being widely adopted in relatively younger electrochemical technologies and in laboratory-scale cells, its application and physical interpretation on commercial LIB systems are still less consolidated.<sup>[14]</sup> The EIS has been used to study cycling and calendar

Dr. C. Rabissi, G. Sordi, Prof. A. Casalegno  
Department of Energy  
Politecnico di Milano  
Via Lambruschini 4, 20156 Milano, Italy

A. Innocenti  
Electrochemistry Group 1  
Helmholtz Institute Ulm (HIU)  
Helmholtzstraße 11, 89081 Ulm, Germany

A. Innocenti  
Karlsruhe Institute for Technology (KIT)  
76131 Karlsruhe, Germany  
E-mail: alessandro.innocenti@kit.edu

 The ORCID identification number(s) for the author(s) of this article can be found under <https://doi.org/10.1002/ente.202000986>.

© 2021 The Authors. Energy Technology published by Wiley-VCH GmbH. This is an open access article under the terms of the Creative Commons Attribution-NonCommercial License, which permits use, distribution and reproduction in any medium, provided the original work is properly cited and is not used for commercial purposes.

DOI: 10.1002/ente.202000986

aging,<sup>[16–18]</sup> the influence of operative conditions on degradation,<sup>[19–21]</sup> and the effect of manufacturing variations on the operation.<sup>[22]</sup> Nevertheless, the results are almost exclusively interpreted with equivalent circuit models (ECM), which mimic the operation of the battery with a network of circuit elements.<sup>[23]</sup> Despite being very popular because of their simplicity and their fast computational time, these methods only provide limited insights regarding the physical behavior of the battery, due to the phenomenological similarity between the electrical elements and the processes occurring in the device. Moreover, they lack in accuracy when the LIB undergoes different load profiles from the one used for the fitting, at different operating conditions and degradation levels.

On the other side, mechanistic models can be powerful in reproducing the physical operation of the battery, because they combine a set of electrochemical, thermal, and mechanical partial differential equations (PDEs).<sup>[24]</sup> Being physics-based, they enable accurate results under wide operating conditions with a strong link to the actual properties of the LIB. Among these, the most widely adopted physical model is the Doyle–Fuller–Newman pseudo-2D (P2D) electrochemical model.<sup>[25]</sup> Although its core has been developed about 30 years ago, this model and its uncountable modifications are still widely adopted in the literature because of the good compromise between physical soundness and computational cost. Starting from the P2D model, there has been the development of simpler formulations, such as the single-particle model,<sup>[26–28]</sup> and of more complex ones, such as the coupled electrochemical–electric–thermal 3D model.<sup>[29,30]</sup> Nevertheless, the simultaneous solution of these PDEs involves a significant computational effort, requiring a tradeoff between accuracy and time.

Also, analytical formulations of physics-based EIS models have been developed to improve simulation performance, adopting several simplifying assumptions that allow the reduction of the PDEs to ordinary equations.<sup>[31–36]</sup> The hypothesis of linearity of the battery response during the EIS and the use of the Fourier transform allow the development of reliable and convenient formulations. Nevertheless, such simplifications, neglecting the solid diffusion of lithium in the particles or the dependency on the lithium concentration of the model parameters, can hinder the validity of results if compared with a full-scale numerical model, especially in the low-frequency impedance region. Moreover, these analytical models can be used only to reproduce the EIS, and not for the battery charge/discharge or dynamic operation simulation, limiting the model flexibility.

However, in both numerical and analytical physics-based formulations, the large number of free parameters can be hard to estimate in their value which, for many cases, can still be debated and unconsolidated, as demonstrated by very broad ranges emerging from the literature. This may lead to problems of over- and under-fitting of the experimental data, weakening the reliability of the simulations outside of the training dataset.<sup>[37]</sup>

To consolidate a physical interpretation of the EIS, it is necessary to understand how the measurement is affected by the operating conditions (ambient temperature and battery SOC) and by the physical parameters that describe the battery in the model. There are many tools to investigate the sensitivity of a model to its parameters,<sup>[38]</sup> but, in general, the most adopted methodologies are: 1) one-factor-at-time (OFAT): in an OFAT analysis, the model parameters are set to nominal values, and they are varied one at a time while keeping the others fixed. The advantages of the OFAT analysis are

its simplicity, its relatively low computational cost, and its ability to show well the mechanistic relations among the model outputs and inputs. The drawbacks are that interactions among different inputs are not explored, and that the information that the OFAT analysis gives are more qualitative. 2) Global sensitivity analysis (GSA): in a GSA, a more rigorous statistical approach is used, because it is based on the variance of the model output with respect to a great number of combinations that the model parameters can assume. A GSA can unveil the effect of interactions among the model parameters, and it can give statistically sound quantitative information on the sensitivity of each of them, assigning an index based on the variance analysis. Nevertheless, a GSA requires a great number of model runs to get a suitable sample of model outputs. Also, the effects of poorly sensitive parameters might be lost, because they could be hidden by the impact of more sensitive ones.<sup>[30]</sup>

Aiming to a systematic discretization of parameters effect on the impedance response, an OFAT sensitivity analysis appears as the optimal choice, being performable with reasonable computational effort on the full-scale P2D model while providing valuable results. In the literature, it is possible to find several examples of sensitivity analysis on LIB models: on ECM,<sup>[39–41]</sup> on the single-particle model,<sup>[27,42,43]</sup> on the proper P2D model,<sup>[44,45]</sup> and also on a coupled electrochemical–electrical–thermal model.<sup>[30]</sup> However, all the reported sensitivity analyses have been performed only on charge/discharge curves or on combinations of current inputs, such as simple driving cycles.

For what concerns the EIS, Murbach and Schwartz created a large database of EIS simulated with the P2D model,<sup>[46]</sup> to use it as a lookup table in an open-source fitting tool for experimental impedance data, but they did not analyze the sensitivity of the simulated EIS with respect to the model parameters. Lyu et al. performed a partial OFAT sensitivity analysis on the simulated EIS spectra with the P2D model,<sup>[47]</sup> limited to only one unspecified operative condition. Recently, as part of a wider work, Zhou and Huang<sup>[48]</sup> performed a sensitivity analysis of a physics-based analytical formulation for the EIS in a porous electrode in a single operative condition, classifying the model parameters according to their influence on the low- or high-frequency range. Based on this analysis, they proposed a methodology for cell screening and aging monitoring. However, due to its analytical formulation and to its distance from the complexity of the actual battery domain, the analysis, although accurate, is unable of providing indications such as the distinction of positive from negative electrode contributions and the identification of the effect of operative conditions on parameters sensitivity.

Hence, to the best of authors' knowledge, no work in the literature follows a systematic OFAT approach on both operative conditions and battery parameters, aiming to highlight their interdependencies, on a full-scale physical model for EIS applied on the actual configuration of commercial LIBs.

In this work, we systematically simulate impedance spectroscopy in the time domain with a P2D Doyle–Fuller–Newman physical model implemented with the temperature effect, discussing the impact of each physical parameter with particular care on the effect of battery conditions such as temperature and battery SOC. Identifying the frequency range and the operating condition of higher sensitivity for each parameter could enable a physically sound model calibration, contributing to strengthening the application of such a model for battery state analysis.

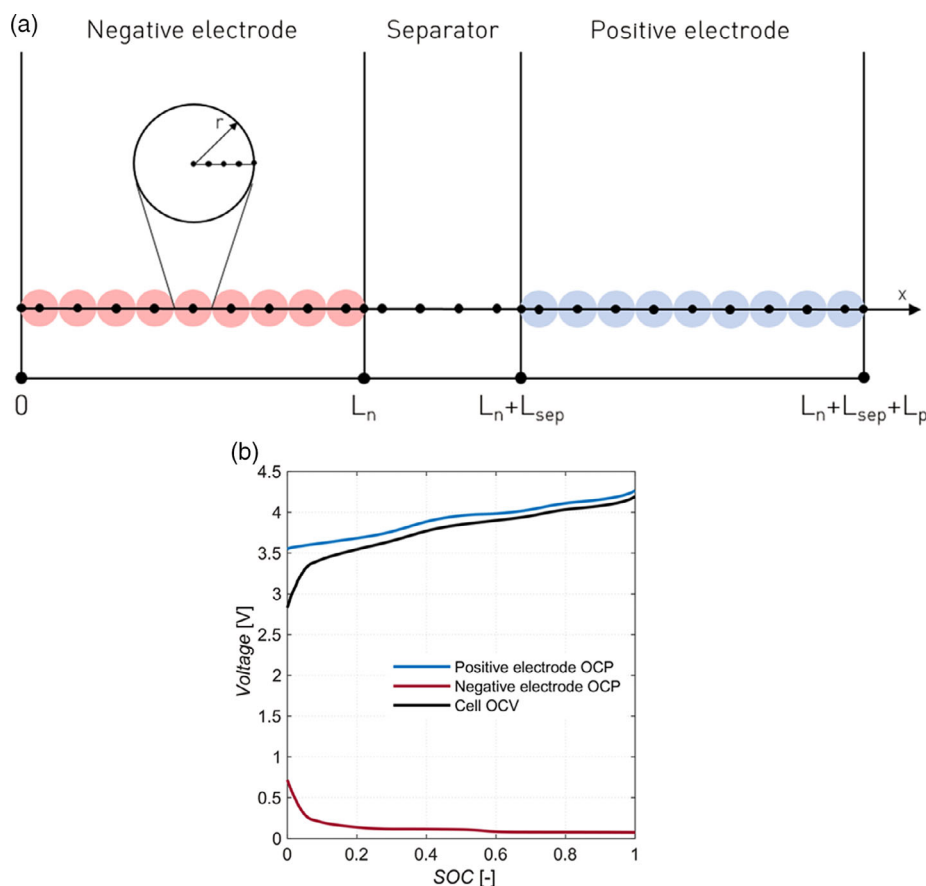


**Figure 1.** a) Schematization of physical model geometrical domain and b) battery  $\Delta V$ -SOC equilibrium curve (OCV), together with corresponding positive and negative electrodes potential curves (OCP).

## 2. Physical Model

The model used in this work is the Doyle–Fuller–Newman P2D formulation, implemented in COMSOL Multiphysics. The battery domain is made of three 1D sub-domains, each characterized by a thickness (Figure 1a): the negative electrode ( $L_n$ ), the separator ( $L_{sep}$ ), and the positive electrode ( $L_p$ ). Each sub-domain is discretized into a set of nodes over its thickness (depth  $x$ ), at which the PDEs are solved. A second radial dimension (radius  $r$ ) is used to model the solid particles of the intercalating materials that constitute the electrodes, and each particle is discretized into several nodes, too. A particle is present at each node along the  $x$ -dimension that belongs to the electrodes' domains.

The overall current  $I$  that is applied to the battery is related to the total current density  $i$  by the electrodes active area  $A_{el}$  through Equation (1)

$$I = A_{el} \times i \quad (1)$$

while the cell voltage  $\Delta V$  is calculated in Equation (2)

$$\Delta V = \varphi_s|_{x=L_n+L_{sep}+L_p} - \varphi_s|_{x=0} - \frac{R_{ext} I}{A_c} \quad (2)$$

as the difference between the solid potentials  $\varphi_s$  at the edges of the battery plus the voltage drop over an external resistance,  $R_{ext}$ ,

referred to the battery cross-sectional area  $A_c$ , which accounts for current collectors and cables resistances.

The battery nominal capacity  $Q_{nom}$  is calculated as the minimum between the capacity of positive and negative electrodes, respectively,  $Q_p$  and  $Q_n$ , which are computed as

$$\begin{cases} Q_p = A_c L_p \varepsilon_{s,am,p} c_{s,max,p} (SOC_{max,p} - SOC_{min,p}) \\ Q_n = A_c L_n \varepsilon_{s,am,n} c_{s,max,n} (SOC_{max,n} - SOC_{min,n}) \end{cases} \quad (3)$$

determined by the cross-sectional area of the battery  $A_c$ , the thickness of the electrodes  $L_p$  and  $L_n$ , the fraction of active materials  $\varepsilon_{s,am,p}$  and  $\varepsilon_{s,am,n}$ , the maximum concentrations of lithium in the electrodes  $c_{s,max,p}$  and  $c_{s,max,n}$ , and the SOC limits of the electrodes. The battery SOC is calculated as the ratio between the actual available charge  $Q$  and the nominal capacity. The open circuit potentials (OCPs) of the electrodes  $E_{ocp}$  are obtained from lookup tables of the electrode potential as a function of the electrode SOC (Figure 1b). The lookup tables are derived from the experimental data of a slow C-rate 0.1 C discharge of the battery sample, which is considered as a good approximation of an equilibrium process.

### 2.1. Solid Potential

The current density in the solid materials  $i_s$  is modeled through Ohm's law in Equation (4)

$$i_s = -\sigma_s^{\text{eff}} \frac{\partial \varphi_s}{\partial x} \quad (4)$$

where the electrode electronic conductivity  $\sigma_s^{\text{eff}}$  is corrected by way of the Bruggeman correlation (Equation (5)) to consider the effect of the tortuosity of the porous medium

$$\sigma_s^{\text{eff}} = \sigma_s \varepsilon_s^{1.5} \quad (5)$$

where  $\varepsilon_s$  is the active fraction of the electrode, occupied by its solid material.

In the boundary conditions of the solid potential (Equation (6)), the electric potential of the solid phase  $\varphi_s$  is set to zero on the left boundary of the negative electrode as a reference potential. As the electrolyte is considered as a pure insulator, no electronic current is present in the separator domain. The overall current is applied at the external boundary of the positive electrode.

$$\begin{cases} \varphi_s|_{x=0} = 0 \\ \frac{\partial \varphi_s}{\partial x}|_{x=L_n^-} = \frac{\partial \varphi_s}{\partial x}|_{x=L_n+L_{\text{sep}}+L_p} = 0 \\ \frac{\partial \varphi_s}{\partial x}|_{x=L_n+L_{\text{sep}}+L_p} = -\frac{I}{A_{\text{el}}} \end{cases} \quad (6)$$

## 2.2. Electrolyte Potential

The current density in the electrolyte  $i_e$  is calculated using Equation (7)

$$i_e = -\kappa_e^{\text{eff}} \frac{\partial \varphi_e}{\partial x} + \frac{2\kappa_e^{\text{eff}} RT}{F} \left(1 + \frac{\partial \ln f_{\pm}}{\partial \ln c_e}\right) (1 - t_0^+) \frac{\partial \ln c_e}{\partial x} \quad (7)$$

where  $\varphi_e$  and  $c_e$  are the potential and the lithium concentration of the electrolyte, respectively,  $\kappa_e^{\text{eff}}$  is the ionic conductivity,  $R$  is the universal gas constant,  $T$  is the temperature,  $F$  is Faraday's constant,  $f_{\pm}$  is the activity coefficient, and  $t_0^+$  is the transference number. The current density in the electrolyte depends on a first term based on Ohm's law that accounts for the migration flux and on a second one that considers the transport of ions due to concentrations gradients. The ionic conductivity  $\kappa_e^{\text{eff}}$  is corrected for the tortuosity of the porous electrode by way of the Bruggeman correlation (Equation (8))

$$\kappa_e^{\text{eff}} = \kappa_e \varepsilon_e^{1.5} \quad (8)$$

where  $\varepsilon_e$  is the fraction of the electrode occupied by the liquid electrolyte.

The activity coefficient  $f_{\pm}$  corrects the concentration-related term, considering the deviation from the dilute solution condition.<sup>[25]</sup> It is expressed as an empirical correlation of the lithium concentration in the electrolyte expressed in  $\text{kmol m}^{-3}$  (Equation (9)), obtained from experimental data on LiPF<sub>6</sub>-based electrolytes<sup>[49]</sup>

$$\begin{aligned} \left(1 + \frac{\partial \ln f_{\pm}}{\partial \ln c_e}\right) &= 1 + c_e \\ &\times \left[ \frac{-1.0189}{(2 \times (1 + 0.9831\sqrt{c_e}))} \left( \frac{1}{\sqrt{c_e}} - \frac{0.9831}{1 + 0.9831\sqrt{c_e}} \right) + 1.584 \right] \end{aligned} \quad (9)$$

The boundary conditions on the electrolyte potential  $\varphi_e$  are listed in Equation (10). The first two conditions imply that there is no electrolytic current at the edges of the battery, where the electrodes adhere to the current collectors. Instead, the last two conditions refer to the continuity of the potential at the interfaces between the electrodes and the separator.

$$\begin{cases} \frac{\partial \varphi_e}{\partial x}|_{x=0} = \frac{\partial \varphi_e}{\partial x}|_{x=L_n+L_{\text{sep}}+L_p} = 0 \\ \varphi_e|_{x=L_n^-} = \varphi_e|_{x=L_n^+} \\ \varphi_e|_{x=L_n+L_{\text{sep}}^-} = \varphi_e|_{x=L_n+L_{\text{sep}}^+} \end{cases} \quad (10)$$

The electrolyte ionic conductivity is computed by means of an empirical correlation, to consider the effects of temperature and the lithium concentration in the electrolyte (Equation (11))

$$\begin{aligned} \kappa_e &= FCE \times 0.1 \\ &\times c_e (-10.5 + 0.0740T - 6.96 \times 10^{-5} T^2 + 0.668c_e - 0.0178c_e T \\ &+ 2.8 \times 10^{-5} c_e T^2 + 0.494c_e^2 - 8.86 \times 10^{-4} c_e^2 T)^2 \end{aligned} \quad (11)$$

It is obtained from experimental data on LiPF<sub>6</sub>-based electrolytes,<sup>[49]</sup> where ionic conductivity factor (FCE) is a calibration constant to be adapted to the specific battery and  $c_e$  is expressed in  $\text{kmol m}^{-3}$ .

## 2.3. Material Balance in the Electrolyte

The mass conservation in the electrolyte is governed by Equation (12).

$$\varepsilon_e \frac{\partial c_e}{\partial t} = \frac{\partial}{\partial x} \left( \varepsilon_e D_e^{\text{eff}} \frac{\partial c_e}{\partial x} \right) - \frac{i_e (\partial t_0^+ / \partial x)}{nF} + a_{j_r} (1 - t_0^+) \quad (12)$$

The left-hand term represents the accumulation of lithium in the electrolyte, which is set equal to the right-hand term, i.e., the flow of lithium in the electrolyte. The latter is composed of the diffusion term, the migration term, and the source term. As the transference number ( $t_0^+$ ) is considered constant, the migration-related term is null. In the separator, this equation holds except for the source term, which is equal to zero due to the absence of reactions. The lithium diffusion coefficient in the electrolyte is corrected for the effect of the tortuosity of the porous electrode through the Bruggeman correlation (Equation (13))

$$D_e^{\text{eff}} = D_e \varepsilon_e^{1.5} \quad (13)$$

The lithium diffusion coefficient in the electrolyte is directly correlated with the ionic conductivity through the Nernst–Planck relationship (Equation (14)),<sup>[50]</sup> hence considering the temperature effect.

$$D_e = \frac{\kappa_e RT}{F^2 c_e} \quad (14)$$

The boundary conditions of Equation (15) define the continuity of the flow of lithium ions in the electrolyte at the interface between the separator and the electrodes, and its absence at the interface with the current collectors.

$$\begin{cases} \left. \frac{\partial c_e}{\partial x} \right|_{x=0} = \left. \frac{\partial c_e}{\partial x} \right|_{x=L_n+L_{sep}+L_p} = 0 \\ -D_e^{\text{eff}} \left. \frac{\partial c_e}{\partial x} \right|_{x=L_n^-} = -D_e^{\text{eff}} \left. \frac{\partial c_e}{\partial x} \right|_{x=L_n^+} \\ -D_e^{\text{eff}} \left. \frac{\partial c_e}{\partial x} \right|_{x=L_n+L_{sep}^-} = -D_e^{\text{eff}} \left. \frac{\partial c_e}{\partial x} \right|_{x=L_n+L_{sep}^+} \end{cases} \quad (15)$$

#### 2.4. Material Balance in the Electrode Particle

At each node  $x$ , the material balance in the electrode particle is also solved over the radius  $r$  as in Equation (16), stating the equality between lithium accumulation and diffusion inside the solid particles, simplified as of spherical geometry of homogeneous radius  $R_p$

$$\frac{\partial c_s}{\partial t} = \frac{1}{r^2} \frac{\partial}{\partial r} \left( D_s r^2 \frac{\partial c_s}{\partial r} \right) \quad (16)$$

where  $c_s$  is the lithium concentration in the electrodes, and  $D_s$  is the diffusion coefficient of lithium in the electrode phase. The lithium diffusion coefficient presents an Arrhenius-type dependence with temperature (Equation (17)), with the activation energy  $EA_D$

$$D_s = D_{s,0} \times e^{\frac{EA_D}{R} \left( \frac{1}{T_0} - \frac{1}{T} \right)} \quad (17)$$

where  $D_{s,0}$  is the reference solid diffusivity measured at the reference temperature  $T_0$ .

The boundary conditions reported in Equation (18) model the equivalence between the lithium flux at the surface of the particle and local reaction lithium flux,  $j_r$ , and the no-flux condition at the center of the sphere due to symmetry.

$$\begin{cases} \left. \frac{\partial c_s}{\partial r} \right|_{r=R_p} = -\frac{j_r}{D_s} \\ \left. \frac{\partial c_s}{\partial r} \right|_{r=0} = 0 \end{cases} \quad (18)$$

#### 2.5. Charge Balance

The derivatives of the current density in the electrolyte and the solid phase are related by Equation (19)

$$\frac{\partial i_e}{\partial x} = -\frac{\partial i_s}{\partial x} = nFaj_r + aC_{dl} \frac{\partial (\varphi_e - \varphi_s)}{\partial t} \quad (19)$$

where  $n$  is the charge of one mole of lithium ions,  $a$  is the active surface-to-volume ratio of spherical particles, and  $C_{dl}$  is the double layer specific capacitance. The first term on the right-hand side of the equation is the reaction current density (also called faradaic current), whereas the second term accounts for the current density in the double layer (also called non-faradaic current).

The sum of the electrolyte and solid current densities gives the total current density applied on the battery (Equation (20))

$$i = i_e + i_s \quad (20)$$

The active surface-to-volume ratio of spherical particles is calculated as in Equation (21)

$$a = 3 \frac{\varepsilon_{s,am}}{R_p} \quad (21)$$

In each electrode and in the separator, the mass balance of the constituents is given by Equation (22)

$$\varepsilon_e + \varepsilon_s = \varepsilon_e + \varepsilon_{s,am} + \varepsilon_{s,i} = 1 \quad (22)$$

where  $\varepsilon_{s,i}$  is the fraction of inactive solid material, i.e., the binder, the conductive additives, passive layers, and electrode material with no electrical contact.

#### 2.6. Electrochemical Reactions

The local reaction current density  $i_r$  generated or consumed through the electrode reactions is determined by means of the Butler–Volmer kinetics, modeled by Equation (23)

$$i_r = i_0 \left[ e^{\left( \frac{\alpha_a F}{RT} \eta \right)} - e^{\left( -\frac{\alpha_c F}{RT} \eta \right)} \right] \quad (23)$$

which relates the current to the overpotential  $\eta$  of the electrochemical reactions, where  $i_0$  is the exchange current density, and  $\alpha_a$  and  $\alpha_c$  are the anodic and cathodic transfer coefficient, respectively. The local reaction current density is related to the local reaction lithium flux  $j_r$  through Faraday's law (Equation (24))

$$i_r = nFj_r \quad (24)$$

The exchange current density  $i_0$ , i.e., the bidirectional current between the electrode and the electrolyte at equilibrium conditions, is expressed as

$$i_0 = Fk \sqrt{(c_{s,max} - c_s)(c_s)} \sqrt{\left( \frac{c_e}{c_{e,ref}} \right)} \quad (25)$$

where  $k$  is the kinetic rate constant, and  $c_{e,ref}$  is the reference lithium concentration in the electrolyte. The concentration-related terms correct the exchange current density according to the availability of lithium in the electrode and in the electrolyte: the lower the concentration of lithium in the electrolyte ( $c_e$ ) and the nearer the concentration in the solid ( $c_s$ ) to the extreme values ( $c_{s,max}$  and zero), the lower the exchange current density. The rate constant  $k$  has an Arrhenius-type dependence with the temperature. Each of the two electrodes' rate constant is coupled to an activation energy  $EA_k$ , with the reference rate constant  $k_0$  measured at the temperature  $T_0$ .

$$k = k_0 \times e^{\frac{EA_k}{R} \left( \frac{1}{T_0} - \frac{1}{T} \right)} \quad (26)$$

Finally, the electrode overpotential  $\eta$  is expressed as in Equation (27)

$$\eta = \varphi_s - \varphi_e - E_{OCP} - i_r R_{film} \quad (27)$$

where  $R_{film}$  represents the specific resistance (in  $\Omega \times m^2$ ) of the interfacial layer on the surface of the active electrode particles, modeled as a dimensionless purely resistive layer. Despite being a relevant simplification, the transport of ions through surface

layers is often difficult to detect in pristine commercial batteries. The solid electrolyte interphases (SEI) can have various compositions and properties;<sup>[51]</sup> its characteristic frequency on the impedance spectrum is debated in the literature,<sup>[52,53]</sup> and its occurrence might be hidden either by the larger charge transfer semicircles or by the porosity effect and the particle radius distribution.<sup>[52]</sup> As this work is not focused on aging, this approach is considered consistent.

Each electrode OCP has an additional term that is a function of temperature (Equation (28)), which derives from the thermodynamic definition of OCP, and it is obtained from lookup tables present in COMSOL

$$E_{\text{OCP}} = E_{\text{OCP},0} + T \frac{\partial E_{\text{OCP}}}{\partial T} \quad (28)$$

The dependences of the film resistances and the electronic conductivities of the electrodes with temperature are considered negligible in the range considered in this work, and hence, they are not included in the model.

The independent variables of the model are  $x$ ,  $t$ , and  $r$ , whereas the dependent variables are  $c_e$ ,  $c_s$ ,  $\varphi_e$ ,  $\varphi_s$ ,  $i_e$ , and  $j_r$ . The starting battery SOC and the temperature are given as an input to the model. A steady-state initialization step is required to set the lithium concentration in the electrodes, such that the available capacity matches the input SOC. The PDEs are solved at each of the  $N$  nodes of the 1D mesh, whereas the solid diffusion PDE is solved in each of the  $M$  nodes inside each of the  $N-N_{\text{sep}}$  electrode spherical particles, where  $N_{\text{sep}}$  is the number of nodes in the separator. Therefore, in each time step,  $5 \cdot N + (N - N_{\text{sep}}) \cdot M$  PDEs are solved. The direct, fully coupled solver uses the nonlinear Newton's method, with the implicit backward differentiation formula for the time stepping.

## 2.7. EIS Simulation

The EIS is based on the application of a sinusoidal current  $I$  (or voltage  $V$ ) input to the battery, measuring the corresponding response over voltage  $V$  (or current  $I$ ). The EIS hypotheses of linearity, stationarity, and causality require the perturbation to be small (generally, the peak-to-peak amplitude is accepted up to 10–15 mV<sup>[14]</sup>) on a fully relaxed open circuit voltage (OCV) condition. The alternate signal frequency  $f$  determines the measured impedance, which will be composed of a real part and an imaginary part

$$\begin{aligned} Z^*(f) &= \frac{V \times e^{i\theta_1(f)}}{i \times e^{i\theta_2(f)}} = Z \times e^{i[\theta_1(f) - \theta_2(f)]} \\ &= Z^* \times \{\cos[\theta(f)] + i \times \sin[\theta(f)]\} \end{aligned} \quad (29)$$

where  $Z^*$  is the module of the specific impedance, measured in  $\Omega \text{ m}^2$ , which represents the ratio between the amplitudes of voltage and current, and  $\theta$  is the phase shift between voltage and current sinusoids. Each frequency stresses a class of phenomena taking place during the battery operation (e.g., Ohmic drop, charge transfer, and diffusion) based on the corresponding characteristic time, enabling an effective separation.

In our work, the impedance response is simulated as a galvanostatic perturbation in the time domain, spanning 30

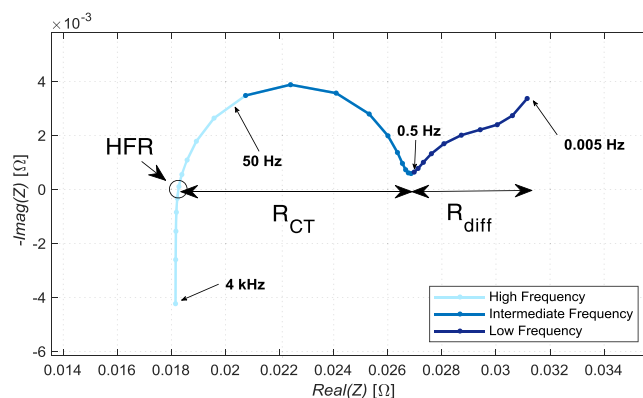


**Figure 2.** Frequency bands partition on a representative EIS spectrum.

logarithmically spaced frequencies between 4000 and 0.005 Hz. After discarding any transient, periods are then elaborated using the fast Fourier transform (FFT) in MATLAB, moving to a frequency domain analysis and enabling the calculation of the impedance value. An example of the resulting spectrum is reported in **Figure 2**, whose frequency bands, ranging from high to low, are highlighted in different colors. The results of the simulations are reported as absolute impedance  $Z$ , measured in  $\Omega$ .

The simulated impedance spectra are corrected to account for the inductive branch at high frequency that is commonly found performing the EIS in batteries due to the inductance of the wires, adding the correction of Equation (30)

$$Z_{\text{corr}}(f) = Z(f) + 2 \times i\pi l f \quad (30)$$

where  $l$  is the value of the inductance of the cables equal to  $1.07 \times 10^{-6}$  H, an average value calculated from the experimental data of this work.

As visible in the picture, several features are recognizable depending on the frequency range, and each resistance associated with the main limiting phenomena can be approximated through simplified equations derived by the linearization of the response of the battery model to an alternating current input, which is allowed by the linearity assumption for the measurement.<sup>[14,31,33]</sup> These formulations, despite not rigorously representing the response of our more complex and complete model, are useful for a qualitative interpretation of the results of the sensitivity analysis and to have a first understanding of the dependencies with temperature and SOC. For a deeper analysis, the reader is referred to the analytical solutions<sup>[31,32]</sup> as supporting tools to the interpretation.

The high-frequency region (from 4 kHz to 50 Hz, light blue in Figure 2) features inductive effects related to external wires and cell windings, pure resistive effects related to the resistance of electrolyte and electrodes, and the eventual onset of features related to SEI. The real impedance in this frequency range is usually indicated as high-frequency resistance (HFR). The HFR approximation is obtained by assuming an infinite frequency of the alternate current input to the battery model<sup>[46]</sup>

$$\text{HFR} \approx \sum_{p,n,\text{sep}} \frac{L}{\kappa_e^{\text{eff}} + \sigma^{\text{eff}}} + R_{\text{film}} + R_{\text{ext}} \quad (31)$$

Hence, it is affected by  $k_e^{\text{eff}}$  (a function of  $T$ , FCE, and  $c_e$  as in Equation (11)), components thickness  $L$ , and film resistance  $R_{\text{film}}$ .

The mid-frequency region (from 50 to 0.5 Hz, blue in Figure 2) is, instead, mainly affected by capacitive features related to charge transfer reactions and double layer effects at anode and cathode, toward the typical minimum in imaginary impedance, whose superimposition generally appears as one regular or elongated semicircle on the Nyquist plot. The linearized charge transfer resistance  $R_{\text{ct}}$  that derives from the Butler–Volmer kinetics (Equation (23)) is inversely proportional to the exchange current density  $i_0$ , present at the denominator (see Equation (25))

$$R_{\text{ct}} \approx \sum_{p,n} \frac{RT}{F^2 k_0 \times e^{\frac{EA_k}{R}(\frac{1}{T_0} - \frac{1}{T})} \times \sqrt{(c_{s,\text{max}} - c_s) \times c_s} \sqrt{\frac{c_e}{c_{e,0}}}} \quad (32)$$

showing a complex dependency on temperature  $T$ , its activation energy  $EA_k$ , and on lithium concentrations in solid and electrolyte ( $c_s$  and  $c_e$ , respectively), driving battery SOC.

The low-frequency region (from 0.5 to 0.005 Hz, dark blue in Figure 2) is known to be mainly affected by diffusion processes, generally appearing as a quasi-linear trait starting from the minimum of the imaginary impedance. The diffusion resistance  $R_{\text{diff}}$  expression is obtained from the linearization of the Butler–Volmer equation in a simplified model, too,<sup>[44]</sup> considering the solid diffusion in the electrode particles (Equation (16) and (23))

$$R_{\text{diff}} \approx \sum_{p,n} \left( \frac{\partial E_{\text{ocp}}}{\partial c_s} \right) \frac{R_p}{F \cdot D_{s,0} \cdot e^{\frac{EA_D}{R}(\frac{1}{T_0} - \frac{1}{T})}} \quad (33)$$

depending on bulk particle radius  $R_p$ , temperature  $T$ , solid diffusivity of lithium in the bulk  $D_{s,0}$ , and its activation energy  $EA_D$  and the derivative of equilibrium potential with respect to lithium concentration in the electrode.

The abovementioned frequency discretization is adopted in the following sections, where the high frequency, mid frequency, and low frequency regions are often, respectively, indicated as HF, MF, and LF, respectively.

### 3. Sensitivity Analysis

The sensitivity analysis has been performed on operating conditions (temperature and SOC), and all the free parameters involved in the P2D model are discussed in Section 2, which have been selected and classified into four categories: geometric, resistance, kinetic, and mass transport-related parameters. For each parameter, the relative variability range has been identified from the literature to explore the sensitivity of a parameter over a range of meaningful values and according to its general knowledge. Following this approach, the width of each range is a consequence of the intrinsic variability of the parameter on one side, e.g., depending on battery materials and design choices, and the uncertainty regarding the value of the parameter in the literature on the other. In this way, unconsolidated parameters, whose value spans entire orders of magnitude across the literature, will be studied in terms of the actual effect on EIS simulation according to such uncertainty. Depending on the width of the identified range, for each parameter, five values are considered (including the

extremes), which are linearly spaced in case the range spans inside the same order of magnitude or logarithmically spaced in case the range spans over multiple order of magnitude. Among the five values, the central one is adopted as the nominal value, which will, hence, be the linear or logarithmical mean value of their range. The simulations are performed following an OFAT approach (as explained in Section 1) changing one parameter at a time while keeping the others at their nominal value. Hence, the overall simulation matrix involves 28 parameters with five values per parameter over 20 combinations of SOC (100%, 75%, 50%, 25%, and 0%) and temperature (−5, 10, 25, and 40 °C), resulting in 2800 combinations.

A complete list of values with their references is provided in **Table 1**, reporting range and nominal value, together with its class and its relative literature references. Instead, in **Table 2**, there is a list of the parameters, which are kept fixed during the simulations.

The choice of the range of the parameters, and hence the specific results, is specifically referred to a commercial battery with lithium–cobalt–nickel–manganese oxide (NMC)/graphite electrodes. Nevertheless, the general trends that are obtained from the following sensitivity analysis are extendable to other chemistries (e.g., lithium-iron-phosphate-based), considering the differences in the typical values of the parameters.

#### 3.1. Quantification of Parameters Sensitivity

To enable a quantitative comparison of the discussed parameters' effect, the sensitivity of the impedance to a change of the value of a parameter  $P_i$  at a given operating condition  $OC_k$  is computed using the standard deviation (SD) of the real and imaginary parts of the impedance over the five simulations  $V_{ij}$ , as follows

$$SD_{i,k,f}^R = \sqrt{\frac{\sum_{j=1}^5 [R(Z)_{i,k,f,j} - \overline{R(Z)}_{i,k,f}]^2}{5}} \quad (34)$$

$$SD_{i,k,f}^I = \sqrt{\frac{\sum_{j=1}^5 [-I(Z)_{i,k,f,j} + \overline{I(Z)}_{i,k,f}]^2}{5}} \quad (35)$$

where  $SD_{i,k,f}^R$  and  $SD_{i,k,f}^I$  are, respectively, the SD of the real and imaginary parts, for the parameter  $i$ , at one of the 20 operating conditions  $k$  and one of the 30 imposed frequencies  $f$ . The impedance values  $R(Z)_{i,k,f,j}$  and  $-I(Z)_{i,k,f,j}$  are computed for each value  $V_{ji}$  of  $P_i$ , and  $\overline{\cdot}$  and  $\overline{\cdot}$  are the arithmetic mean impedance values over the five simulations, calculated as

$$\overline{R(Z)}_{i,k,f} = \frac{\sum_{j=1}^5 R(Z)_{i,k,f,j}}{5} \quad \overline{I(Z)}_{i,k,f} = \frac{\sum_{j=1}^5 -I(Z)_{i,k,f,j}}{5} \quad (36)$$

The SDs are averaged consistently to the frequency ranges discussed in Section 3.1 and reported in Figure 2 as in the following equations

$$\overline{SD}_{i,k}^{R,F} = \frac{\sum_f SD_{i,k,f}^R}{10} \Big|_{F=H,M,L} \quad \overline{SD}_{i,k}^{I,F} = \frac{\sum_f SD_{i,k,f}^I}{10} \Big|_{F=H,M,L} \quad (37)$$

where  $H$ ,  $M$ , and  $L$  refer, respectively, to the high- (4000–59 Hz), medium- (59–0.54 Hz), and low-frequency (0.54–0.005 Hz) band. This approach aims to discretizing the parameter effect

**Table 1.** List of varied parameters, indicating the category and the investigated range with references.

Parameter	Anode		Separator/Electrolyte/Cell		Cathode		Class	Reference
	Nominal	Range	Nominal	Range	Nominal	Range		
$C_{dl} [F m^{-2}]$	1	0.02–50	–	–	1	0.02–50	Kinetics (K)	[60,61]
$k_0 [m s^{-1}]$	$1 \times 10^{-9}$	$1 \times 10^{-10}$ – $1 \times 10^{-8}$	–	–	$1 \times 10^{-9}$	$1 \times 10^{-10}$ – $1 \times 10^{-8}$	K	[27,44]
$EA_k [J mol^{-1}]$	$4 \times 10^4$	$2 \times 10^4$ – $6 \times 10^4$	–	–	$4 \times 10^4$	$2 \times 10^4$ – $6 \times 10^4$	K	[27,44,61]
$\sigma_s [S m^{-1}]$	316	10–10 000	–	–	3.16	0.1–100	Resistances (R)	[50,55,56]
$R_{film} [\Omega m^2]$	$3.16 \times 10^{-3}$	$1 \times 10^{-3}$ – $1 \times 10^{-2}$	–	–	$3.16 \times 10^{-4}$	$1 \times 10^{-3}$ – $1 \times 10^{-2}$	R	[44,58]
$c_{e,0} [mol m^{-3}]$	–	–	1200	800–1600	–	–	R	[27,44]
FCE [–]	–	–	0.387	0.100–1.500	–	–	R/Mass transport (MT)	[49,50,62]
$D_{s,0} [m^2 s^{-1}]$	$1.58 \times 10^{-13}$	$5 \times 10^{-14}$ – $5 \times 10^{-13}$	–	–	$3.16 \times 10^{-13}$	$1 \times 10^{-14}$ – $1 \times 10^{-13}$	MT	[50,65–67]
$EA_D [J mol^{-1}]$	$4 \times 10^4$	$2 \times 10^4$ – $6 \times 10^4$	–	–	$4 \times 10^4$	$2 \times 10^4$ – $6 \times 10^4$	MT	[27,44,61]
$t_0^+ [–]$	–	–	0.350	0.300–0.400	–	–	MT	[49,50,62]
$R_p [m]$	$6.75 \times 10^{-6}$	$1 \times 10^{-6}$ – $1.25 \times 10^{-5}$	–	–	$6.75 \times 10^{-6}$	$1 \times 10^{-6}$ – $1.25 \times 10^{-5}$	Geometry (G)	[61,63,64]
$\epsilon_e [–]$	0.375	0.325–0.425	0.600	0.550–0.650	0.375	0.325–0.425	G	[61,63,64]
$\epsilon_{s,am} [–]$	0.500	0.450–0.550	–	–	0.450	0.400–0.500	G	[61,63,64]
$L [m]$	$4 \times 10^{-5}$	$2 \times 10^{-5}$ – $6 \times 10^{-5}$	$2.25 \times 10^{-5}$	$1.25 \times 10^{-5}$ – $3.25 \times 10^{-5}$	$4 \times 10^{-5}$	$2 \times 10^{-5}$ – $6 \times 10^{-5}$	G	[61,63,64]
$A_c [m^2]$	–	–	0.1953	0.15–0.25	–	–	G	[27,44,61]

**Table 2.** List of fixed parameters with references.

Parameter	Anode	Separator/Electrolyte/Cell	Cathode	Reference
$SOC_{min} [–]$	0.049	–	0.125	Estimated
$SOC_{max} [–]$	0.850	–	0.870	Estimated
$c_{s,max} [mol m^{-3}]$	31 000	–	37 035	[27,44]
$Q_{nom} [mAh]$	–	2600	–	Assumed
$\alpha_c [–]$	0.5	–	0.5	Assumed
$\alpha_e [–]$	0.5	–	0.5	Assumed
$T_0 [K]$	298.15	298.15	298.15	Assumed
$l [H]$	–	$1.07 \times 10^{-6}$	–	Estimated
$R_{ext} [\Omega \cdot m^2]$	–	0.003	–	Estimated
$\eta [–]$	–	1	–	Assumed

on each timescale, improving the identifiability and distinction of the role of each parameter.

Instead, to obtain a general indicator useful for a global comparison of the average sensitivity of the model to all the parameters, all the SDs associated with each parameter  $i$  can be averaged over the frequencies  $f$  and the operative conditions  $k$  in two lumped values, calculated as

$$\overline{SD}_i^R = \frac{\sum_k \sum_f SD_{i,k,f}^R}{600} \quad \overline{SD}_i^I = \frac{\sum_k \sum_f SD_{i,k,f}^I}{600} \quad (38)$$

Finally, for every parameter, the maximum values of average SDs  $\overline{SD}_{i,k}^{R,F}$  and  $\overline{SD}_{i,k}^{I,F}$  are identified among all the operative conditions and the frequency ranges. The conditions  $OC_{i,max}^R$  and  $OC_{i,max}^I$  (at which the respective  $\overline{SD}_{i,max}^R$  and  $\overline{SD}_{i,max}^I$  are identified) are the ones where the impacts of a variation of the parameter on the imaginary and real impedance are maximized, useful in case of an experimental calibration.

## 4. Results and Discussion

### 4.1. Effect of Operating Conditions

When performing EIS tests on commercial batteries, due to the abovementioned hypothesis constraining the oscillation amplitude, the only degrees of freedom are the ambient temperature and the battery SOC. These operating conditions sensibly affect the impedance response of the battery, and hence, it is important to highlight and discuss their effect on the different mechanisms involved.

The impact of ambient temperature (10–25 to 40 °C, at 50% SOC) and of battery SOC (1–25–50–70–100% SOC, at 25 °C) on simulated EIS are shown in **Figure 3a,b**, respectively.

Regarding temperature effect (**Figure 3a**), it is evident a sensible increase in impedance with decreasing temperature, affecting the entire frequency range of the measurement and resulting in a combined translation and elongation of the EIS spectra. The HFR increase observed in the high-frequency region is consistent with Equation (30) because of the temperature dependence of  $\kappa_e^{eff}$  (Equation (11)). The  $R_{ct}$  growth, which drives the impedance increase at intermediate frequency, is consistent with Equation (31), due to the dependence of the rate constant with the temperature ( $T$ ), primarily following an Arrhenius law dependence at the denominator, prevailing over the direct dependence at the numerator. Hence, enhancing the kinetics of the electrochemical reactions and promoting the diffusion of lithium ions in the electrolyte and the bulk of the electrodes,<sup>[50]</sup>  $R_{ct}$  and the HFR decrease as the ambient temperature increases. This is generally coupled with a shift toward higher frequencies of the corresponding mechanisms (**Figure S1**, Supporting Information), which is shown as a shift of local maximum and minimum of the imaginary impedance. This fact suggests enhanced conduction phenomena, due to the improved mobility



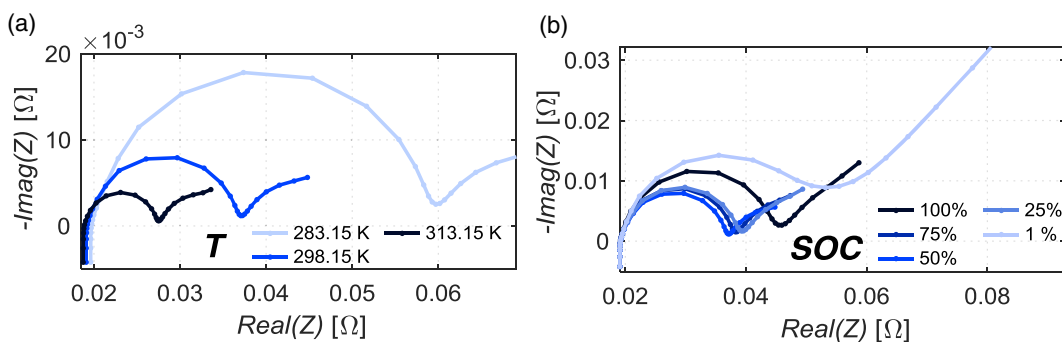


**Figure 3.** Effect of a) temperature and b) SOC variation on simulated EIS spectra.

of the lithium ions and the improved kinetic of the electrochemical reactions.<sup>[50]</sup> The low-frequency region of the spectra, instead, is only slightly affected by the temperature variation.

Concerning the SOC effect (Figure 3b), it appears to affect mainly the impedance spectra at mid-low frequency, which reaches its minimum value at intermediate SOC and grows toward extreme SOC values. Indeed, being SOC directly related to lithium concentration in the electrodes, it affects the exchange current density value, and, in turn,  $R_{ct}$  (Equation (31)). Consequently, there is a minimum of  $R_{ct}$  at intermediate SOC values, while it grows at the extremes, where  $i_o$  decreases. Second, the diffusion resistance  $R_{diff}$  magnitude (Equation (32)), dominating low-frequency region, increases with larger particles (higher particle radius  $R_p$ ), with lower bulk diffusivity ( $D_{s,0}$ ) and lower temperature ( $T$ ), conditions hindering the diffusion of lithium in the electrode. It also depends on the slope of the electrode OCP ( $\frac{\partial E_{ocp}}{\partial c_s}$ ), which usually grows at extreme SOC values according to the materials intercalation curves

(see Figure 1b),<sup>[33]</sup> particularly for the negative electrode at low SOC.

To permit a qualitative validation of the simulated impedance trends with respect to battery operating conditions (temperature and SOC), **Figure 4** reports experimental data for two different types of experimental samples (high power and high energy of slightly different capacity) in the same operative conditions of the simulated EIS spectra (for the description of the adopted measurements protocols, the reader is referred to the Experimental Section of this article). It is worth to stress that the nominal values of all the parameters reported in Table 1, at which simulations reported in Figure 3 are performed, have been identified from the literature to maximize the generality of the discussion and results. Only the consistency of simulated battery capacity with the proposed experimental references has been obtained by means of electrodes frontal area, scaling the order of magnitude of impedance value.

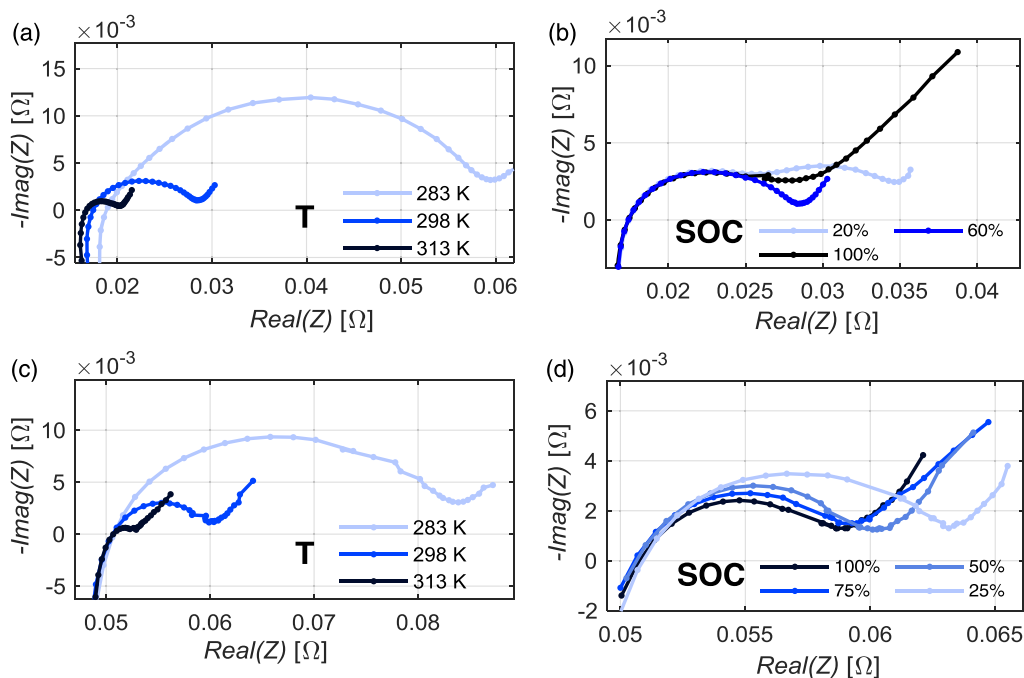


**Figure 4.** a,c) Effect of temperature and b,d) SOC variation on experimental EIS spectra for a,b) high-power and c,d) high-energy commercial samples, respectively.

As clear from the reported experimental spectra, a qualitative agreement with the simulated EIS data previously discussed is manifest, demonstrating as first, general results, the consistency of both the nominal values identified from the literature and of the model in reproducing the effects of temperature and SOC variations on the battery response, which heterogeneously affects EIS spectra. Despite the different structure of the batteries, a general growth of  $R_{ct}$  is manifest with decreasing temperature and for extreme SOC values. In particular, at lower temperature, a decrease in the characteristic frequencies of mechanisms is also observed and followed by a rightward translation of the impedance spectra (Figure S2 and S3, Supporting Information). At very low SOC, the impedance contribution of the graphite anode becomes dominant at all frequencies, showing a significant increase in both charge transfer resistance and the diffusive tail, whereas no relevant changes of the characteristic frequencies of the phenomena can be appreciated. It is worth to mention a feature, which appears at 20% SOC of the high-power sample (Figure 4b), where the experimental EIS shows a second semicircle appearing at low frequency overlapped with the diffusion impedance, which is not reproduced in the model. The theoretical exchange current density relation with the electrode lithium concentration (Equation (25)) does not explain such trend, which could be indeed related to the behavior of layered cathode materials, constituting the positive electrode of experimental samples (as mentioned in the relative section), when close to the fully lithiated state (i.e., at battery SOC close to zero). When approaching this region, further lithium intercalation is known to promote switch the behavior of the material from the one of a semi-metal to the one of a semi-conductor,<sup>[52,54]</sup> featuring more sluggish kinetics due to poor conduction capabilities, which could explain the sudden impedance increase. This strongly nonlinear phenomenon is not considered in the formulation of our model, nor of interest for the scope of this work.

In general, the increased magnitude of the impedance at lower temperatures and extremes SOCs will result in a higher sensitivity of the model to the parameters (see Table S14 and S15, Supporting Information). Despite this similarity, it is possible to appreciate some peculiar trends with the operative conditions for certain parameters. These non-uniformities, which will be explained in the subsequent sections, are useful to identify and potentially isolate which parameters have the higher impact on the impedance spectra at different conditions of temperature, SOC, and frequency.

#### 4.2. Geometry

This category of parameters includes the quantities that describe the physical structure of the battery: solid particle radii, electrode porosity and active material fraction, components thickness, and the battery surface. The effect on the impedance spectra is reported in Figure 5.

The absolute impedance  $Z$  (measured in  $\Omega$ ) is related to the specific impedance  $Z^*$  (measured in  $\Omega \text{ m}^2$ ) by the active area of the electrode  $A_{el}$  (Equation (39)), that is computed as the product between the whole volume of the electrode ( $L \cdot A_c$ ) and the specific active area  $a$ .

$$Z = \frac{Z^*}{A_{el}} = \frac{Z^*}{L \cdot A_c \cdot a} = Z^* \times \frac{R_p}{L \cdot A_c \cdot 3\epsilon_{s,am}} \quad (39)$$

Each of the resistances, approximated through Equation (31)–(33), has to be divided by  $A_{el}$ . In this way, Equation (39) can effectively highlight the role of the geometrical parameters of the battery in the determination of the impedance. First, the positive and negative electrode particle radii ( $R_{p,p}$ ,  $R_{p,n}$ ) have a significant effect on several phenomena involved in battery operation, directly affecting the specific active surface of the electrodes (Figure 5a,b). Hence, an increase in the radius determines a general growth of impedance. In particular,  $R_{p,n}$  has a considerable impact on the HFR, because the negative electrode has a relatively high film resistance due to the presence of a thick SEI layer, visible as a horizontal translation of spectra from high-frequency region.  $R_{p,p}$  is not as impactful, because the film resistance associated with the interfacial layer at the cathode is usually negligible in commercial LIBs because of the good anodic stability of the common organic liquid electrolyte. Similarly, at intermediate frequencies, the charge transfer resistance grows as the radius increases. The diffusion impedance has a quadratic dependence on the particle radius, because this impedance increases with the radius both in Equation (33) and (39). At first, the approximation indicates that the diffusion impedance changes with the radius only when the derivative of the OCP is different from zero. In fact, the low-frequency impedance does not vary with  $R_{p,n}$ , because the graphitic electrode is in an almost zero-slope OCP zone (i.e., a phase transition) at the considered SOC (for comparison, in Figure S4, Supporting Information, it is shown the influence of  $R_{p,n}$  at 1% SOC). Instead, Figure 5b shows a remarkable increase in the diffusion impedance with  $R_{p,p}$  because of the sloping positive electrode potential in that SOC region.

The positive and negative electrode active material fraction ( $\epsilon_{s,am,p}$ ,  $\epsilon_{s,am,n}$ ) account for the fraction of the electrode volume available for electrochemical reactions. As a general consideration, as the sensitivity analysis is performed following an OFAT approach, a reduction of the active material fraction of one electrode basically determines its downsizing, e.g., lower electrode capacity, leaving the other unaffected. It means that this electrode faces a higher load, i.e., increased local current density. Both the effects on the charge transfer resistance and the diffusion resistance are analogous to the ones of the electrode thicknesses (Figure 5c,d), which are discussed in the following. However, according to the variability range adopted in this analysis, the extent of the impact of active material fraction changes is very little.

The thickness of the positive and of the negative electrode ( $L_p$ ,  $L_n$ ) significantly affect the performances of the electrodes, as displayed in Figure 5e,f. A higher thickness increases the volume and the capacity of the electrode, thus decreasing the magnitude of the overall impedance (Equation (39)). Hence, we observe a relevant variation of the real part of the impedance due to the voltage drop for the bulk resistance of the electrode and of the charge transfer semicircle. These parameters also induce a nonlinear behavior of the low-frequency region, consistent with a variation of the slope of the OCP: indeed, a change in the thickness of one electrode affects its lithium concentration at

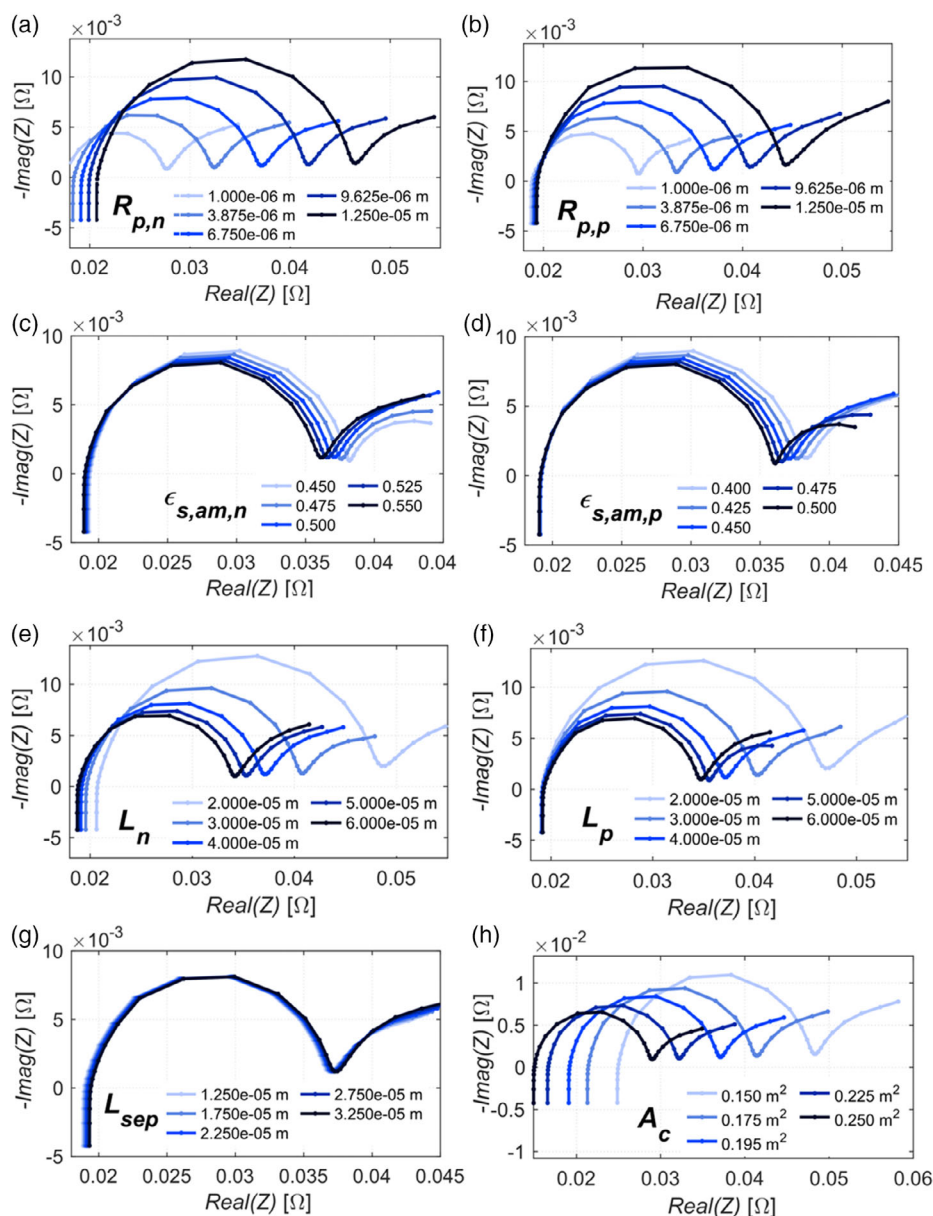


**Figure 5.** Variation of the impedance spectra due to the geometric parameters: a, b) particle radius of negative electrode/positive electrode ( $R_{p,n}$ ,  $R_{p,p}$ ), c, d) active material fraction of negative electrode/positive electrode ( $\epsilon_{s,am,n}$ ,  $\epsilon_{s,am,p}$ ), e–g) thicknesses of negative electrode/positive electrode/separator ( $L_n$ ,  $L_p$ , and  $L_{sep}$ ), and h) contact area ( $A_c$ ). The simulations are performed at 25 °C and 50% SOC if not indicated otherwise in the figures.

the investigated battery SOC and, hence, the position on the OCP curve (Figure 1a).

The thickness of the separator ( $L_{sep}$ ) shows just a slight effect on the HFR and the diffusion impedance (Figure 5g). A thicker separator increases the resistance in the battery due to the electrolyte conductivity because of a longer pathway between the two electrodes which lithium ions must cross. The same reasoning can be applied to the increased diffusion impedance. Nevertheless, the sensitivity of this parameter appears negligible with respect to the selected value range on the battery impedance response.

The battery contact area ( $A_c$ ) affects the response of the device at all the frequencies. Similarly to the previous discussions,

different contact area implies a battery of different volume and capacity. Therefore, the smaller the area, the smaller the battery and the higher the absolute impedance  $Z$  at a prescribed load condition (Figure 5h), but the specific impedance  $Z^*$  keeps the same. In fact, the smaller the contact area, the higher the current density, but the lower the overall impedance, the higher the voltage response to the alternate current, too, with the same magnitude (Equation (29)).

The porosities of the electrodes and the separator ( $\epsilon_{e,p}$ ,  $\epsilon_{e,n}$ ,  $\epsilon_{e,sep}$ ), not shown in Figure 5 because of their negligible effect, act on the effective ionic conductivity of the electrolyte through the Bruggeman correlation (Equation (13)). Therefore, an increase

in porosity brings to lower resistance of the electrolyte because of the lower tortuosity of the path for the lithium ions transport. Nevertheless, this effect has shown a very limited influence on the overall impedance for all the three parameters, and it can be considered negligible for the common range of porosities found in commercial batteries (Figure S5–S7, Supporting Information).

### 4.3. Resistances

This class of parameters includes the electronic conductivities and the film resistances of the two electrodes, the ionic conductivity of the electrolyte, and the starting lithium concentration of the electrolyte. Sensitivity analysis of these parameters is reported in Figure 6.

The electronic conductivities ( $\sigma_{s,p}$ ,  $\sigma_{s,n}$ ) of the two electrode materials impact the HFR. With a lower value of these parameters, in Figure 6a,b, a rightward shift of the spectrum is observed, which is associated with a higher electronic bulk resistance. Nevertheless, the range of variability of these two parameters in commercial LIBs is such that the actual impact on the EIS is quite limited, especially for the negative electrode. For graphite anodes, the electronic conductivity can be in the order of  $1000\text{--}10\,000\text{ S m}^{-1}$  due to the inherently conductive nature of the material.<sup>[55]</sup> Cathode materials

usually have quite poor electronic conductivity, but the use of carbon-based conductive additives enhances the conductivity and allows a uniform utilization of the positive electrode,<sup>[56]</sup> globally determining a low sensitivity for this parameter.

The film resistances ( $R_{\text{film,p}}$ ,  $R_{\text{film,n}}$ ) of both the positive and the negative electrode determine pure resistive effects in the resulting impedance spectra. In Figure 6c,d, it is possible to recognize a horizontal rightward shift of the entire spectrum, easy to be identified with a direct influence on the HFR value (Equation (31)), due to the approximation of the SEI to a 0D resistive layer. The positive electrode film resistance, attributed to the cathode electrolyte interface layer, has a very low effect on the HFR because of its typically very low values in commercial LIB cathodes.<sup>[57]</sup> Instead, the solid electrolyte interface layer resistance, which is present on the graphitic electrode, is at least one order of magnitude higher than the cathode one, resulting in a significant influence on the shape of the impedance spectrum. A more accurate estimation of the film resistances is quite challenging, due to the variable nature of the layer, which depends on the electrolyte mixture and on the characteristics of the anode graphite.<sup>[58]</sup>

A variation of lithium concentration in the electrolyte ( $c_{e,0}$ ) affects the entire impedance spectrum, because it determines the value of the ionic conductivity and the lithium diffusion

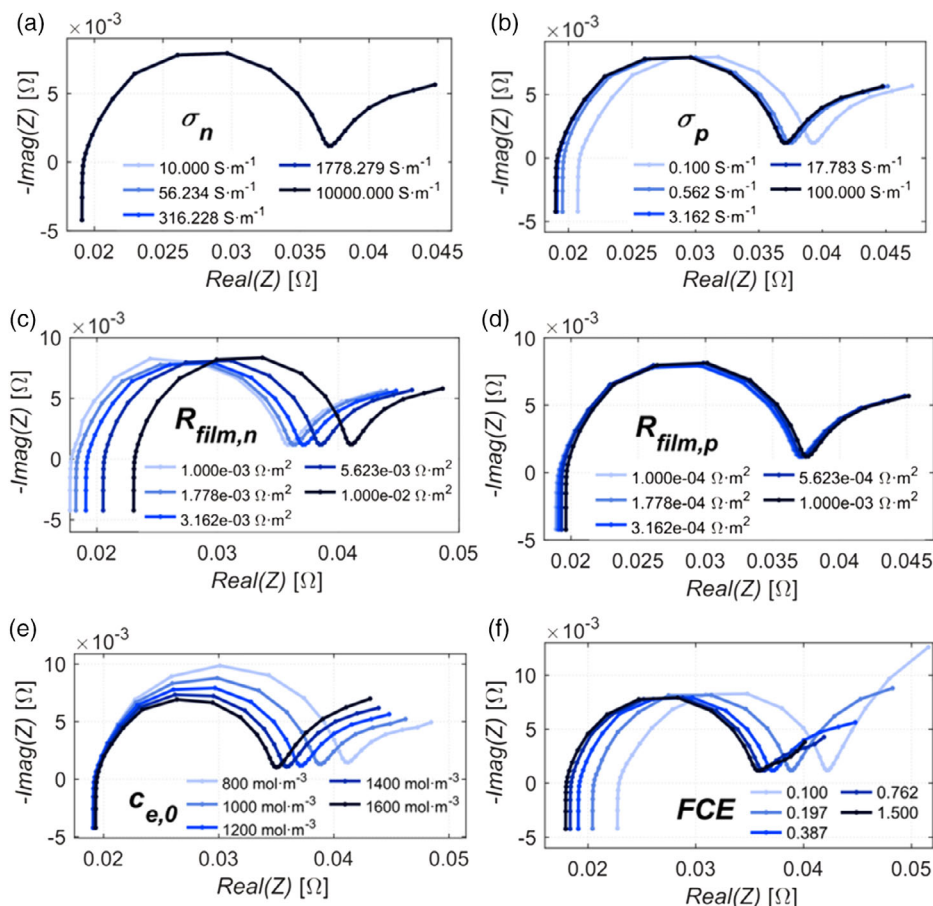


**Figure 6.** Variation of the impedance spectra due to the resistive parameters: a,b) electric conductivity of negative electrode/positive electrode ( $\sigma_n$ ,  $\sigma_p$ ), c, d) film resistance of negative electrode/positive electrode ( $R_{\text{film,p}}$ ,  $R_{\text{film,n}}$ ), e) electrolyte concentration ( $c_{e,0}$ ), and f) conductivity factor (FCE). The simulations are made at 25 °C and 50% SOC if not indicated otherwise in the figures.

coefficient of the electrolyte (Figure 6e). The HFR has its minimum value at  $1200 \text{ mol m}^{-3}$ , which is the optimal concentration that maximizes the ionic conductivity (Equation (11)). Nevertheless, the overall variation of the HFR is relatively small if compared with the effect of other parameters. The charge transfer resistance increases as  $c_{e,0}$  decreases, because the lower availability of lithium in the electrolyte hinders the electrochemical reactions at the electrodes. The diffusion resistance slightly decreases with the decrease in  $c_{e,0}$  because of the higher value assumed by the lithium diffusion coefficient in the electrolyte, according to Equation (14).

The FCE, which is used as a scaling factor of the ionic conductivity of the electrolyte (Equation (11)), influences greatly the value of the HFR, as shown in Figure 6f on the high-frequency region of the spectra. In fact,  $\kappa_e$  determines the bulk resistance of the battery (Equation (31)), and according to the different mixtures of solvents used in the liquid electrolyte formulation, the ionic conductivity can vary considerably according to the viscosity and the dielectric constant of the constituents, and the respective molar ratio.<sup>[59]</sup> The variation of the low-frequency impedance will be discussed in Section 4.5.

#### 4.4. Kinetics

This category comprises the double layer capacitances, the rate constants of the reactions, and their activation energies. The effect on the impedance spectra is reported in Figure 7.

The rate constants ( $k_{0,p}$ ,  $k_{0,n}$ ) are the parameters that overall have the highest influence on the shape of the impedance spectrum, mostly due to the high variability range used in this work, which stems from the high uncertainty in the estimation of rate constant that is found in the literature. The charge transfer resistance grows up to an order of magnitude between the highest and the lowest values of these parameters (Figure 7a,b). This is a consequence of Equation (25), where kinetic constants affect the exchange current density of the reaction and, as a result, the  $R_{ct}$  (Equation (32)), which is inversely proportional to the kinetic constants. This effect becomes even more evident at low temperature because of the exponential relationship between the rate constants and the operation temperature, given by the Arrhenius behavior of Equation (26) and introduced in Section 4.1. Moreover, from Figure S8 and S9, Supporting Information, it is possible to notice how an increase in these parameters induces

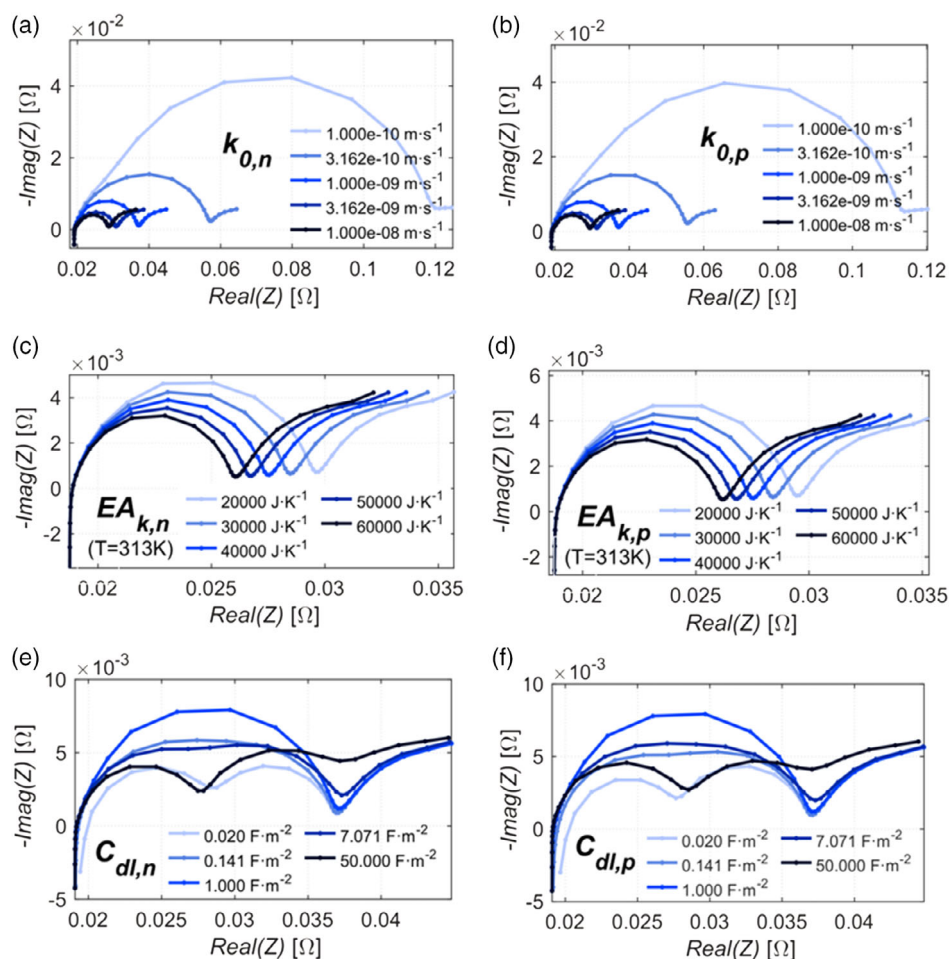


**Figure 7.** Variation of the impedance spectra due to the kinetic parameters: a,b) rate constant ( $k_{0,n}$ ,  $k_{0,p}$ ) and c,d) the corresponding activation energy ( $EA_{k,n}$ ,  $EA_{k,p}$ ) of negative electrode/positive electrode, and e,f) double layer capacitance of negative electrode/positive electrode ( $C_{dl,n}$ ,  $C_{dl,p}$ ). The simulations are made at  $25^\circ\text{C}$  and 50% SOC if not indicated otherwise in the figures.

a shift toward a higher frequency of the charge transfer resistance imaginary peak. This is consistent with the physics of the phenomenon, because higher rate constants imply faster kinetics; thus, the electrochemical reaction can reach its full extent even with a higher frequency of the pulse that induces the reaction.

The activation energies of the rate constants ( $EA_{k,p}$ ,  $EA_{k,n}$ ) are accountable for the variations of the rate constants at different temperatures. A higher activation energy of the rate constant implies a stronger dependence of the rate constant itself with temperature. Of course, at the reference temperature, the activation energy does not influence on the value of the rate constant  $k$ , which will be equal to  $k_0$ . The farther the temperature from the reference value, the stronger the influence of the value of the activation energy on the final rate constant, hence its sensitivity toward EIS spectra. As displayed in Figure 7c,d, performed at 40 °C to show the spectrum variation, these parameters have the same effect of the rate constants, but the sensitivity has a lower magnitude consistently with the relatively smaller range of variability identified for this parameter.

The double layer capacitances ( $C_{dl,p}$ ,  $C_{dl,n}$ ) quantify the capacity of the double layer formed at the solid–liquid interface between the electrode and the electrolyte, specific to the particle surface. In the battery modeling literature, such parameter is often set to an arbitrary value, or even neglected,<sup>[29,60]</sup> as a consequence of the limited experimental determinability, which is mainly relying, at the moment, on fitting of EIS spectra with electric circuit models.<sup>[61]</sup> From the results of our simulation, it is clear how the capacitance of the double layer of both electrodes sensibly affects the shape of the impedance spectra shown in Figure 7e,f. Higher values of  $C_{dl}$  induce a delay in the occurrence of the charge transfer, sensibly shifting it to lower frequencies. As an example, a change from 0.02 to 50 F m<sup>-2</sup> of the negative electrode double layer capacitance shifts the imaginary impedance peak of the charge transfer resistance from  $4 \times 10^2$  to  $2 \times 10^{-1}$  Hz (Figure S10 and S11, Supporting Information). This is consistent with the concept of double layer, which involves the charge/discharge of the liquid–solid interface, which is in parallel connection with the faradaic current involved in the charge transfer reaction.<sup>[60]</sup> As their sum is the total current flowing in the battery (Equation (19)), a higher fraction of current allocated to the double layer charge/discharge will temporarily decrease the charge transfer rate, resulting in a longer time for the electrochemical reaction to reach its full extent. Such an increase in the characteristic time delay will, hence, manifest in the EIS spectrum as a shift toward lower frequencies of the imaginary peak. The difference between the effect of a variation of the positive and of the negative double layer capacitance is quite negligible in terms of the magnitude of the shift of the charge transfer frequency. When the two parameters have about the same value, the impedance spectra are characterized by a single large semi-circle, while the more they differ, the more the spectra decompose into two smaller semi-circles of the two separated electrodes. The one with the lower  $C_{dl}$  value is situated at higher frequencies, whereas the one with the higher  $C_{dl}$  value sits at lower frequencies.

#### 4.5. Mass Transport

This class includes the lithium diffusion coefficient in the electrode materials, the respective activation energies to account for

temperature variations, the transference number of the electrolyte, and the diffusion coefficient of lithium in the electrolyte (which is shown by means of the FCE). The sensitivity analysis of these parameters over is reported in Figure 8.

The lithium diffusion coefficients in the electrode materials ( $D_{s,0,p}$ ,  $D_{s,0,n}$ ) play a key role in determining the rate of the diffusive flux of matter between the center and the surface of the particles (Equation (16)). A reduction of this coefficient determines a slower lithium diffusion in the solid bulk, until this process becomes the bottleneck of the charge/discharge of the battery, especially at high current operations. In the impedance spectra, the features related to diffusion, as shown in Figure 8a,b, for the negative (at low SOC to enhance the effect) and the positive electrode, respectively, are present at low frequency (indicatively, below 1 Hz). As the diffusivity decreases, two effects are observed. First, the diffusion impedance grows, according to Equation (33). The magnitude of this growth is strictly related to the slope of the OCP curve. When the slope is low, as in the positive electrode at intermediate SOC or during the phase transitions of graphite, the variation of the impedance in the low-frequency range with the diffusion coefficient is limited or nearly null (Figure S12, Supporting Information). Instead, when the slope is high, as in graphite in the OCP trait with high slope at low SOC, the increase can be greatly enhanced (Figure 8a reports EIS spectra at very low SOC to enhance the discussed effect). This relationship between SOC and diffusion resistance can be highlighted because of the use of actual OCP curves of the positive and negative electrodes. Second, the onset of diffusion-limiting performance shifts at a higher frequency, with an extension of the frequency range of the diffusion resistance, up to interfering with charge transfer-related semicircle.

The activation energies of the diffusion coefficients ( $EA_{D,p}$ ,  $EA_{D,n}$ ) are responsible for the variation of the rate diffusion coefficients with temperature. The effect is analogous to the one of the rate constant activation energies (Figure 8c,d): a higher value of this parameter causes a higher variation of the diffusion coefficient when the temperature changes; hence, its impact is more sensitive at lower temperatures. The impact of  $EA_{D,p}$  and  $EA_{D,n}$  is relevant in the same operative condition where the one of the diffusion coefficients is significant too (Figure S13, Supporting Information).

The transference number ( $t_0^+$ ) is the ratio between the current carried out by the cation  $Li^+$  over the overall electrolyte current  $i_e$ . In Equation (8), it appears in the concentration-related term. Indeed, when the applied perturbation has a low frequency and diffusion starts to play a role, a variation of the transference number affects the distribution of charge in the battery, modifying the voltage response to current. However, as shown in Figure 8e, the effect on the simulated impedance spectra is rather limited, because the transference number range for the liquid electrolytes of commercial batteries is quite narrow.<sup>[49,50,62]</sup>

The diffusion coefficient of lithium in the electrolyte is modified through the FCE, affecting both mass transport as well as resistance parameters category, because there is a direct physical relation between  $D_e$  and  $\kappa_e$  through Equation (14). Looking at the low-frequency region of the impedance spectra of Figure 8f, a decrease in the FCE (and, hence, in the diffusion coefficient) determines a steep increase in the diffusion-related resistance. This phenomenon is not considered in Equation (33), because

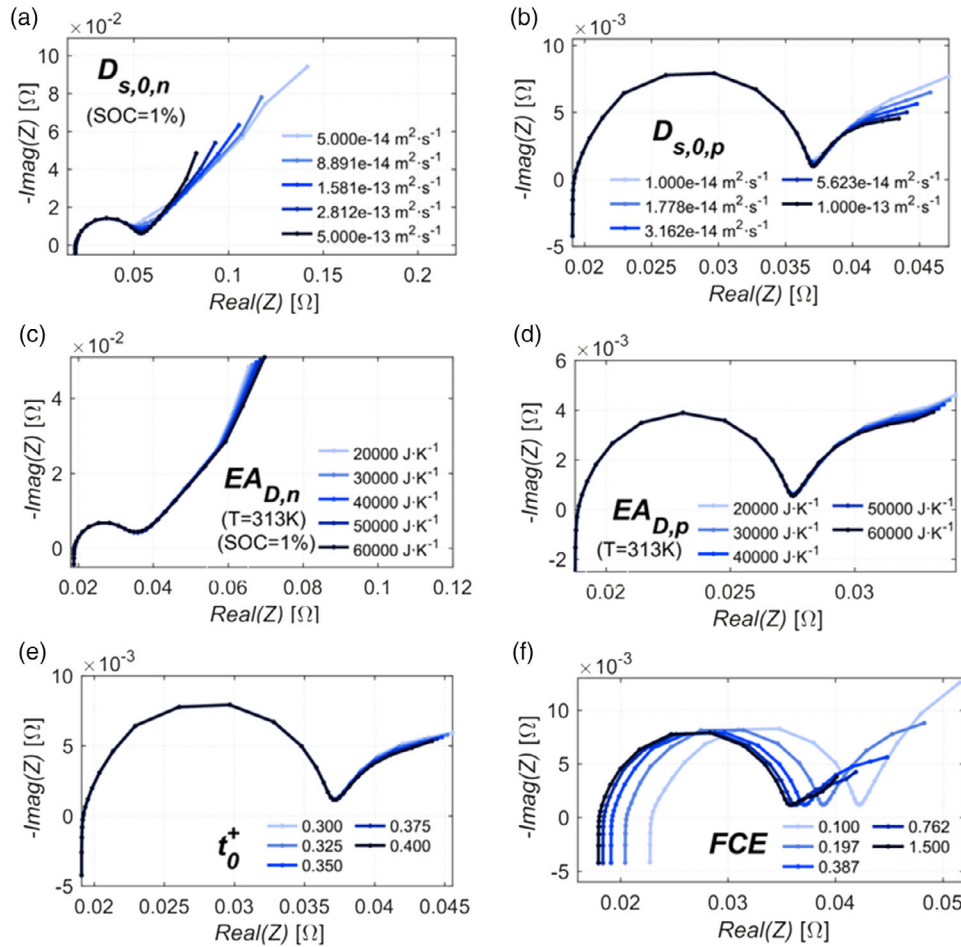


**Figure 8.** Variation of the impedance spectra due to the mass transport parameters: a,b) solid diffusivity ( $D_{s,0,n}$ ,  $D_{s,0,p}$ ) and c,d) corresponding activation energy ( $EA_{D,n}$ ,  $EA_{D,p}$ ) of negative electrode/positive electrode, e) transference number ( $t^+$ ), and f) FCE. The simulations are made at 25 °C and 50% SOC if not indicated otherwise in the figures.

this approximation only considers the diffusion of lithium in the solid. The effect of the lithium diffusion coefficient in the electrolyte appears to be unaffected by the slope of the OCP, because this parameter acts on the distribution of lithium in the electrolyte and, hence, on the one of the electrolyte potentials. Through the electrolyte potential, the voltage response of the battery to the current input is changed (Equation (27)), and hence, the impedance changes too.

#### 4.6. Summary of the Sensitivity Analysis

To discretize the results, a classification of the physical parameters is performed based on the SD values, calculated as described in Section 3.1, according to the comparison with the multiples of threshold values of the sensitivity  $SD_{\min}^R$  and  $SD_{\min}^I$ , defining their degree of significance. The limit values for real and imaginary impedance are set to be both 0.5 mΩ. Therefore, the sensitivity of the EIS spectra to a variation of the  $i$ th parameter is classified according to these criteria

$$\text{Insensitive(-) if } \overline{SD}_i^{\max} < SD_{\min} \quad (40)$$

$$\begin{aligned} \text{Poorly sensitive(*) if } \overline{SD}_i > SD_{\min} \text{ and } \overline{SD}_i \\ < 3 \times SD_{\min} \text{ or } \overline{SD}_i^{\max} > 3 \times SD_{\min} \end{aligned} \quad (41)$$

$$\begin{aligned} \text{Sensitive(**) if } \overline{SD}_i > 3 \times SD_{\min} \text{ and } \overline{SD}_i \\ < 10 \times SD_{\min} \text{ or } \overline{SD}_i^{\max} > 10 \times SD_{\min} \end{aligned} \quad (42)$$

$$\text{Highly sensitive(***) if } \overline{SD}_i > 10 \times SD_{\min} \quad (43)$$

The results of the SD-based quantification of parameters' impact on the impedance response are summarized in **Table 3**, also reporting the conditions of maximum sensitivity. For a detailed visualization of results, the reader is also referred to the Supporting Information, where  $\overline{SD}_i^{R/I,SOC}$ ,  $\overline{SD}_i^{R/I,T}$ , and  $\overline{SD}_i^{R/I,f}$  are tabulated in Table S14–S16, Supporting Information, respectively, enabling the comparison of the model sensitivity to the parameters with respect to the operating conditions ( $T$ , SOC) and the frequency range ( $f$ ).

**Figure 9** shows the values of the lumped SDs of the parameters over all the operating conditions and frequency bands,  $\overline{SD}_i^R$

**Table 3.** Average and maximum SDs for each parameter, both for the imaginary and the real impedance. The reported operative conditions refer to the condition in which the maximum SDs are found. If a parameter is in the “insensitive” category, the maximum SD operative condition is not reported because of the lack of significance.

Parameter	Class	Real impedance				Imaginary impedance			
		$\overline{SD}_i^R$ [mΩ]	$\overline{SD}_{i,max}^R$ [mΩ]	$OC_{i,max}^R$	Class	$\overline{SD}_i^I$ [mΩ]	$\overline{SD}_{i,max}^I$ [mΩ]	$OC_{i,max}^I$	Class
$C_{i,p}$	K	5.7	27.8	−5 °C, 100% SOC, MF	***	2.9	10.6	−5 °C, 100% SOC, MF	***
$C_{dl,n}$	K	7.1	48.4	−5 °C, 1% SOC, LF	***	3.3	16.2	−5 °C, 1% SOC, LF	***
$k_{0,p}$	K	25.9	169.0	−5 °C, 100% SOC, LF	***	9.0	56.3	−5 °C, 100% SOC, LF	***
$k_{0,n}$	K	27.9	200.6	−5 °C, 1% SOC, LF	***	10.5	83.6	−5 °C, 1% SOC, LF	***
$c_{e,0}$	R	2.7	19.5	−5 °C, 1% SOC, LF	**	0.764	3.5	−5 °C, 100% SOC, MF	*
FCE	R/MT	2.8	4.8	−5 °C, LF	**	0.547	0.990	10 °C, LF	*
$t_0^+$	MT	0.056	0.215	–	–	0.062	0.247	–	–
$\sigma_p$	R	0.823	0.892	−5 °C, HF	*	0.022	0.062	–	–
$\sigma_n$	R	0.009	0.057	–	–	0.001	0.043	–	–
$R_{p,p}$	G	7.5	45.7	−5 °C, 100% SOC, LF	***	2.2	10.8	−5 °C, 100% SOC, MF	**
$R_{p,n}$	G	9.7	83.1	−5 °C, 1% SOC, LF	***	2.9	34.0	−5 °C, 1% SOC, MF	**
$D_{s,0,p}$	MT	0.422	3.4	−5 °C, 100% SOC, LF	*	0.504	4.9	−5 °C, 100% SOC, LF	*
$D_{s,0,n}$	MT	0.724	15.7	−5 °C, 1% SOC, LF	**	0.804	20.0	−5 °C, 1% SOC, LF	**
$R_{film,p}$	R	0.022	0.035	–	–	0.095	0.529	–	–
$R_{film,n}$	R	1.8	1.9	HF	**	0.016	0.098	–	–
$\epsilon_{e,p}$	G	0.135	0.257	–	–	0.031	0.108	–	–
$\epsilon_{e,n}$	G	0.125	0.257	–	–	0.036	0.109	–	–
$\epsilon_{e,se}$	G	0.066	0.095	–	–	0.012	0.060	–	–
$EA_{k,p}$	K	4.6	47.1	−5 °C, 100% SOC, LF	**	1.3	9.0	−5 °C, 100% SOC, MF	**
$EA_{k,n}$	K	5.1	64.1	−5 °C, 1% SOC, LF	***	1.6	15.9	−5 °C, 1% SOC, MF	**
$EA_{D,p}$	MT	0.189	2.7	−5 °C, 100% SOC, LF	*	0.236	3.8	−5 °C, 100% SOC, LF	*
$EA_{D,n}$	MT	0.565	19.1	−5 °C, 1% SOC, LF	**	0.680	25.1	−5 °C, 1% SOC, LF	**
$\epsilon_{s,am,p}$	G	1.1	10.5	−5 °C, 1% SOC, LF	*	0.434	2.8	−5 °C, 1% SOC, LF	*
$\epsilon_{s,am,n}$	G	1.0	8.2	−5 °C, 100% SOC, LF	*	0.366	2.3	−5 °C, 100% SOC, LF	*
$A_c$	G	8.5	42.1	−5 °C, 1% SOC, LF	***	1.8	13.6	−5 °C, 1% SOC, LF	**
$L_p$	G	6.0	40.2	−5 °C, 1% SOC, LF	***	2.0	13.6	−5 °C, 1% SOC, MF	**
$L_n$	G	7.1	54.6	−5 °C, 1% SOC, LF	***	2.4	25.2	−5 °C, 1% SOC, LF	**
$L_{sep}$	G	0.232	0.364	–	–	0.037	0.122	–	–

and  $\overline{SD}_i^I$ . The different colors highlight the four categories, in which the parameters are divided. Despite the averaging steps, this chart can provide a visual representation of the overall sensitiveness of the simulated EIS spectra to the variation of the model parameters.

Summarizing the results of the sensitivity analysis with respect to the frequency ranges, at high/medium-high frequency, the most sensitive parameters are found to be the FCE and the negative film resistance  $R_{film,n}$  (and, hence, also the negative particle radius  $R_{p,n}$ ) determining the active surface of the negative electrode. All these parameters contribute to the value of the HFR, and their variations produce a similar effect, i.e., a horizontal shift of the whole spectrum.

The medium-low/low-frequency range is instead dominated by the kinetic rate constants, their activation energies, and the particle radii, which affect the charge transfer resistance value  $R_{ct}$ . Instead, the effect of a variation in diffusion-related

parameters in the very low-frequency range is not as impactful as a variation of the charge transfer-related parameters in the mid-low-frequency range. Nevertheless, the impact of the solid diffusion coefficients and their activation energies becomes more important at the extremes of the SOC, where both the electrodes are closer to the maximum and minimum concentration of lithium allowed by the material, and the slopes of the electrodes' OCP curves are higher. This is shown by the relatively high difference between their average and maximum SD values.

The kinetic parameters, particularly the rate constants and the double layer capacitances, show to have the highest sensitivity over the EIS spectra, sharing the main effect of increasing imaginary impedance at medium frequency causing an enlargement of  $R_{ct}$  feature and must be carefully evaluated. However, they can be identified with their peculiar, sensible effect on the frequency of the imaginary impedance peak, causing its shift. Regarding the double layer capacitances, even though their relevant effect



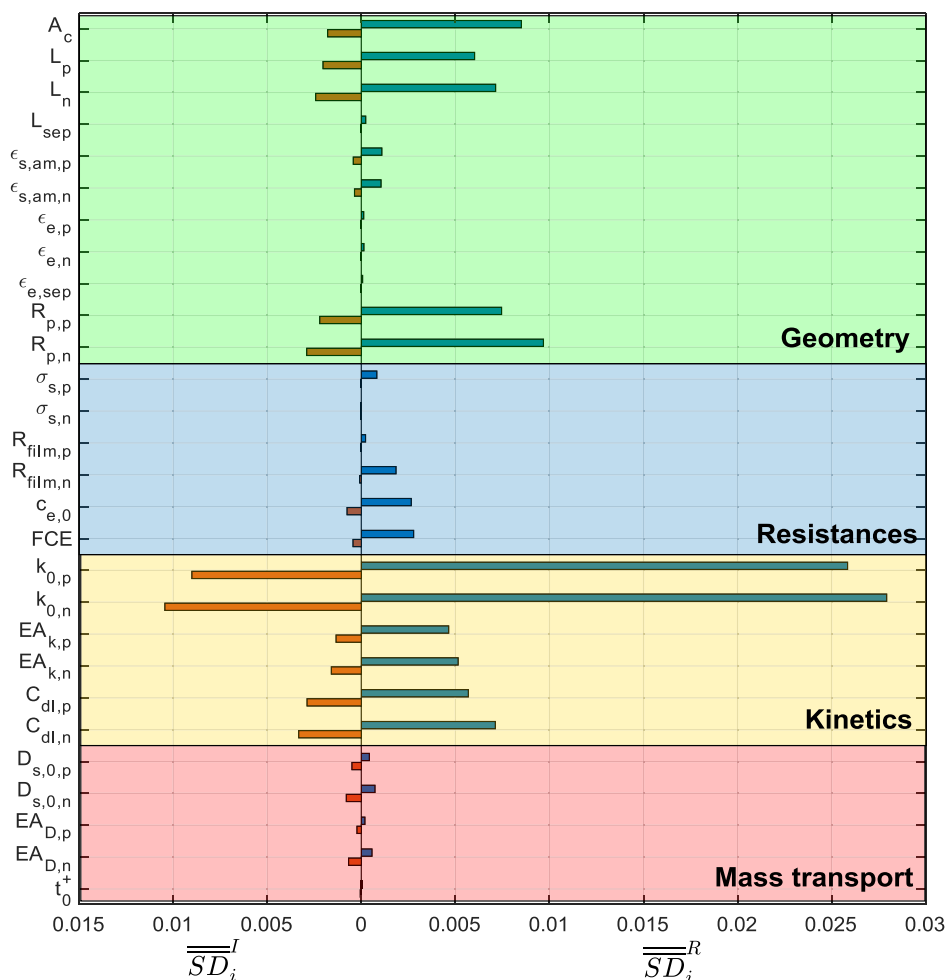


**Figure 9.**  $\overline{SD}_i^R$  and  $\overline{SD}_i^I$  of all the parameters, blue and orange bars, respectively.

is observed on all the frequency range, they feature the highest influence on the value of the imaginary component of the impedance at high frequency and low temperature (for the SD averaging with respect to the frequency range, the reader is referred to Table S16, Supporting Information).

Almost all the geometric parameters affect the impedance response of the battery in a sensible way, as evident from the high SD associated with them in Table 3. Therefore, the knowledge of the value of these parameters is advisable for a proper interpretation of EIS data with the battery model, also considering their easy and direct measurability by means of nondestructive imaging techniques or through battery samples dismantling.<sup>[63,64]</sup>

Regarding operational conditions, being  $R_{ct}$  and  $R_{diff}$  resistances of each electrode function of lithium concentration and of OCP curve slope, the sensitivity of negative electrode parameters (such as  $C_{dl}$ ,  $k_0$ ,  $R_p$ ,  $D_{s,0}$ , and  $\epsilon_s$ ) generally grows at low battery SOC, whereas the opposite can be stated for positive electrode parameters. This is a promising feature for enhancing the distinction of the two electrodes' contributions in an experimental calibration of model parameters. Moreover,  $EA_D$  and  $EA_k$  show an increased sensitivity at lower temperature, according to the Arrhenius dependencies from temperature of both diffusive

and kinetic processes, showing a favorable condition for calibration purposes. Therefore, most of the involved parameters feature an increased impact on EIS response at lower temperatures.

Interestingly, 40% of the parameters, 12 out of 28, are evaluated poorly sensitive or insensitive to the EIS simulations, as shown from the very low SD values (both average and maximum), such as the transference number, the separator thickness, the porosities of the components, the anodic electronic conductivity, and the positive film resistance. In the range of values analyzed in this work, typical of a commercial high-power LIB, a variation of these parameters has a negligible effect on the simulated spectra. Therefore, fitting the experimental EIS data with a physical model, their value can be directly assumed from the literature without significantly losing accuracy.

## 5. Conclusion

In this work, a comprehensive sensitivity analysis of 28 physical parameters of the P2D model has been performed as a function of temperature and battery SOC for a total of 2800 combinations, aiming to understand and differentiate the impact of such parameters over operating conditions and frequency range.

First, the presented P2D model is verified to be able to reproduce the effect of temperature and SOC on EIS spectra with physical consistency with experimental measurements.

Second, physical parameters have been shown to determine a sensibly different effect on the impedance response of LIBs. In particular: 1) overall, the sensitivity is increased at lower temperature and high and low SOC for the positive and negative electrode, respectively, enabling a beneficial distinction of the contributions; 2) the kinetic rate constants are the most impacting parameters at mid-to-low frequency, and therefore, their calibration is of utter importance for model reliability; 3) the double layer capacitances effects mostly appear on the imaginary part of the impedance, causing the elongation of the charge transfer resistance-related feature or its separation in two distinguishable semicircles; 4) geometric parameters such as particles radii and electrodes thicknesses have a generally sensible impact on EIS spectra; therefore, their knowledge, considering the relative ease for a physical measurement through battery dismantling, is strongly advised to increase model reliability; 5) the FCE has a relevant impact on HFR feature and diffusion resistance, affecting the entire frequency range; and 6) 40% of the parameters are demonstrated to have a minor effect on EIS spectra in the selected range and could be suitably excluded from the calibration, easing the process. The less impactful parameters are transference number, separator thickness, components' porosity, anodic electronic conductivity, and the positive film resistance.

Hence, to aid a comprehensive and physically sound experimental calibration of P2D model, it is advisable to rely on EIS measurements, spanning from high to low frequency range, performed at high and low values of SOC and temperature to enable a substantial distinction of negative and positive electrodes contributions and temperature dependencies of kinetic and transport properties.

This analysis permits to deepen the physical-based understanding of LIB impedance response, enabling an optimized experimental calibration of the DFN model. This could partially overcome the overfitting issue related to a large number of involved parameters, aiding the adoption of EIS for diagnostics of performance and degradation of batteries.

## 6. Experimental Section

**Experimental Setup:** The test bench adopted in this work has been ad-hoc developed with a modular structure, to provide highly flexible and low uncertainty operation. An NI DAQ USB 6218 board is adopted to provide redundant voltage measurement on the battery samples and to provide high-speed measurement of voltage oscillation to increase the quality of impedance measurements up to very high frequency. An Autolab PGSTAT30 potentiostat/galvanostat provided with a frequency response analyzer board (FRA2) is used for EIS measurement for the sake of repeatability.

The battery samples are operated in a Binder KT 53 thermoelectric chamber (Control temperature uncertainty:  $\pm 0.3$  °C), to provide a highly controlled temperature environment for battery characterization. The superficial temperature of each battery sample is measured during operation by means of type K thermocouples, whose measure is acquired using an NI CDAQ 9211 as temperature acquisition board.

**Experimental Measurements:** The impedance is measured at 10, 25, and 40 °C. Before every measurement, the battery is charged up to 100% SOC at 25 °C, following a constant current–constant voltage (CC–CV) procedure with CC C-rate 1C and CV at 4.2V. The CV phase is hold until

the current drops below 0.04 C. Then, the temperature of the chamber is varied if needed. After the end of the charging procedure and the eventual temperature change, the battery is left at rest for 12 h to accommodate any electrochemical and thermal relaxation phenomena. The impedance spectroscopy is performed at 100% SOC; then, the battery is discharged by the desired time to reach the target SOC at 0.2 C. After 24 h, the EIS is performed at the target SOC.

The EIS is performed at OCV in galvanostatic mode: the battery voltage response to a current sinusoidal oscillation is measured, varying frequencies in 40 logarithmically spaced values between 10 kHz and 50 mHz. The imposed current waveform is applied for at least 1 s or three full periods to ensure steady state. The amplitude of the applied current is in the 100–200 mA range, according to the operating temperature, to obtain a voltage oscillation lower than 10 mV, respecting the linearity condition of the EIS. Measurement consistency is verified by the retrospective use of Kramers–Kronig transform, and impedance values that do not satisfy such relations are discarded.

**Battery Samples:** In this work, nominal simulations are compared against experimental measurements performed on two samples of commercial batteries: 1) High-power samples: 2.6 Ah Sony US26650VT. The positive electrode is constituted of an unspecified blend of NMC and lithium-manganese oxide (LMO), coupled with a graphite (C) negative electrode. 2) High-energy samples: 2.25 Ah Sony US18650V3. The positive electrode is constituted of NMC, coupled with a graphite (C) negative electrode.

For both samples, the binder is polyvinylidene fluoride, whereas the liquid electrolyte is an unknown mixture of organic solvents and LiPF<sub>6</sub> as lithium salt.

## Supporting Information

Supporting Information is available from the Wiley Online Library or from the author.

## Acknowledgements

The research leading to these results has received funding from the Energy for Motion initiative of Politecnico di Milano as part of Energy department recognition as Department of Excellence 2018-2020 from Italian Ministry of Education, Universities and Research (MIUR). The authors would like to acknowledge the Helmholtz Institute Ulm (HIU) and Karlsruhe Institute of Technology (KIT) for the useful support in the data elaboration tasks. Open access funding enabled and organized by Projekt DEAL.

## Conflict of Interest

The authors declare no conflict of interest.

## Keywords

battery modeling, electrochemical impedance spectroscopy, lithium-ion batteries, sensitivity analysis

Received: November 10, 2020  
Revised: December 3, 2020  
Published online: January 18, 2021

- [1] R. Schmich, R. Wagner, G. Hörpel, T. Placke, M. Winter, *Nat. Energy* **2018**, *3*, 267.
- [2] B. Dunn, H. Kamath, J. M. Tarascon, *Science* **2011**, *334*, 928.
- [3] T. Bunsen, P. Cazzola, L. d'Amore, M. Gerner, S. Scheffer, R. Schuitmaker, H. Signollet, J. Tattini, J. Teter, L. Paoli, *Global EV*

- Outlook 2019*, <https://www.iea.org/reports/global-ev-outlook-2019> (accessed: November 2019).
- [4] Q. Wang, B. Mao, S. I. Stolarov, J. Sun, *Prog. Energy Combust. Sci.* **2019**, *73*, 95.
- [5] D. Hall, N. Lutsey, *ICCT Brief* **2018**, 12.
- [6] J. Vetter, P. Novák, M.R. Wagner, C. Veit, K.-C. Möller, J.O. Besenhard, M. Winter, M. Wohlfahrt-Mehrens, C. Vogler, A. Hammouche, *J. Power Sources* **2005**, *147*, 269.
- [7] A. Barré, B. Deguilhem, S. Grolleau, M. Gérard, F. Suard, D. Riu, *J. Power Sources* **2013**, *241*, 680.
- [8] P. Arora, *J. Electrochem. Soc.* **1998**, *145*, 3647.
- [9] K. Uddin, S. Perera, W. D. Widanage, L. Somerville, J. Marco, *Batteries* **2016**, *2*, 1.
- [10] K. Honkura, K. Takahashi, T. Horiba, *J. Power Sources* **2011**, *196*, 10141.
- [11] V. Laue, O. Schmidt, H. Dreger, X. Xie, F. Röder, R. Schenkendorf, A. Kwade, U. Krewer, *Energy Technol.* **2020**, *8*, 1.
- [12] A. Barai, K. Uddin, M. Dubarry, L. Somerville, A. McGordon, P. Jennings, I. Bloom, *Prog. Energy Combust. Sci.* **2019**, *72*, 1.
- [13] S. Schindler, M. Bauer, M. Petzl, M. A. Danzer, *J. Power Sources* **2016**, *304*, 170.
- [14] N. Meddings, M. Heinrich, F. Overney, J.-S. Lee, V. Ruiz, E. Napolitano, S. Seitz, G. Hinds, R. Raccichini, M. Gaberšček, J. Park, *J. Power Sources* **2020**, *480*, 228742.
- [15] C. Pastor-Fernández, K. Uddin, G. H. Chouchelamane, W. D. Widanage, J. Marco, *J. Power Sources* **2017**, *360*, 301.
- [16] T. P. Heins, N. Schlüter, U. Schröder, *ChemElectroChem* **2017**, *4*, 2921.
- [17] P. S. Sabet, A. J. Warnecke, F. Meier, H. Witzhausen, E. Martinez-Laserna, D. U. Sauer, *J. Power Sources* **2020**, *449*, 227369.
- [18] J. Groot, M. Swierczynski, A. I. Stan, S. K. Kær, *J. Power Sources* **2015**, *286*, 475.
- [19] M. Ecker, P. Shafiei Sabet, D. U. Sauer, *Appl. Energy* **2017**, *206*, 934.
- [20] A. Barai, K. Uddin, J. Chevalier, G. H. Chouchelamane, A. McGordon, J. Low, P. Jennings, *Sci. Rep.* **2017**, *7*, 1.
- [21] S. S. Zhang, *J. Power Sources* **2006**, *161*, 1385.
- [22] T. P. Heins, R. Leithoff, N. Schlüter, U. Schröder, K. Dröder, *Energy Technol.* **2020**, *8*, 1.
- [23] S. Nejad, D. T. Gladwin, D. A. Stone, *J. Power Sources* **2016**, *316*, 183.
- [24] U. Krewer, F. Röder, E. Harinath, R. D. Braatz, B. Bedürftig, R. Findeisen, *J. Electrochem. Soc.* **2018**, *165*, A3656.
- [25] T. F. Fuller, M. Doyle, J. Newman, *J. Electrochem. Soc.* **2019**, *141*, 1.
- [26] X. Han, M. Ouyang, L. Lu, J. Li, *J. Power Sources* **2015**, *278*, 802.
- [27] C. Edouard, M. Petit, C. Forgez, J. Bernard, R. Revel, *J. Power Sources* **2016**, *325*, 482.
- [28] A. M. Bizeray, J. H. Kim, S. R. Duncan, D. A. Howey, *IEEE Trans. Control Syst. Technol* **2019**, *27*, 1862.
- [29] N. Lin, F. Röder, U. Krewer, *Energies* **2018**, *11*, 1.
- [30] N. Lin, X. Xie, R. Schenkendorf, U. Krewer, *J. Electrochem. Soc.* **2018**, *165*, A1169.
- [31] J. Huang, J. Zhang, *J. Electrochem. Soc.* **2016**, *163*, A1983.
- [32] S. Devan, V. R. Subramanian, R. E. White, *J. Electrochem. Soc.* **2004**, *151*, A905.
- [33] J. P. Meyers, M. Doyle, R. M. Darling, J. Newman, *J. Electrochem. Soc.* **2000**, *147*, 2930.
- [34] G. Sikha, R. E. White, *J. Electrochem. Soc.* **2007**, *154*, A43.
- [35] M. D. Levi, D. Aurbach, *J. Phys. Chem. B* **2004**, *108*, 11693.
- [36] R. W. J. M. Huang, F. Chung, E. M. Kelder, *J. Electrochem. Soc.* **2006**, *153*, A1459.
- [37] J. C. Forman, S. J. Moura, J. L. Stein, H. K. Fathy, *J. Power Sources* **2012**, *210*, 263.
- [38] G. ten Broeke, G. van Voorn, A. Ligtenberg, *Jasss* **2016**, *19*, 1.
- [39] S. Zhao, D. A. Howey, in *IEEE Veh. Power Propuls. Conf. VPPC 2016 – Proc. 2–5*, IEEE, Piscataway, NJ **2016**, pp. 1–4.
- [40] F. Guo, G. Hu, P. Zhou, T. Huang, X. Chen, M. Ye, J. He, *Int. J. Energy Res.* **2019**, *43*, 9013.
- [41] X. Lai, S. Wang, S. Ma, J. Xie, Y. Zheng, *Electrochim. Acta* **2020**, *330*, 135239.
- [42] A. P. Schmidt, M. Bitzer, Á. W. Imre, L. Guzzella, *J. Power Sources* **2010**, *195*, 5071.
- [43] S. Santhanagopalan, Q. Guo, R. E. White, *J. Electrochem. Soc.* **2007**, *154*, A198.
- [44] L. Zhang, C. Lyu, G. Hinds, L. Wang, W. Luo, J. Zheng, K. Ma, *J. Electrochem. Soc.* **2014**, *161*, A762.
- [45] N. Jin, D. L. Danilov, P. M. J. Van den Hof, M. C. F. Donkers, *Int. J. Energy Res.* **2018**, *42*, 2417.
- [46] M. D. Murbach, D. T. Schwartz, *J. Electrochem. Soc.* **2018**, *165*, A297.
- [47] C. Lyu, W. Cong, H. Liu, L. Zhang, in *Progn. Syst. Heal. Manag. Conf. PHM-Harbin 2017 – Proc.*, IEEE, Harbin, China, **2017**, pp. 1–8.
- [48] X. Zhou, J. Huang, *J. Energy Storage* **2020**, *31*, 101629.
- [49] L. O. Valo/en, J. N. Reimers, *J. Electrochem. Soc.* **2005**, *152*, A882.
- [50] M. Park, X. Zhang, M. Chung, G. B. Less, A. M. Sastry, *J. Power Sources* **2010**, *195*, 7904.
- [51] S. J. An, J. Li, C. Daniel, D. Mohanty, S. Nagpure, D. L. Wood, *Carbon* **2016**, *105*, 52.
- [52] I. Jiménez Gordon, S. Grugeon, A. Débart, G. Pascaly, S. Laruelle, *Solid State Ionics* **2013**, *237*, 50.
- [53] V. J. Ovejas, A. Cuadras, *Batteries* **2018**, *4*, 1.
- [54] K. M. Shaju, G. V. Subba Rao, B. V. R. Chowdari, *J. Electrochem. Soc.* **2004**, *151*, A1324.
- [55] A. K. Dutta, *Phys. Rev.* **1953**, *90*, 187.
- [56] Y.-H. Chen, C.-W. Wang, G. Liu, X.-Y. Song, V. S. Battaglia, A. M. Sastry, *J. Electrochem. Soc.* **2007**, *154*, A978.
- [57] K. Edström, T. Gustafsson, J. O. Thomas, *Electrochim. Acta* **2004**, *50*, 397.
- [58] C. C. Chang, S. Y. Huang, W. H. Chen, *Energy* **2019**, *174*, 999.
- [59] J. Kalhoff, G. G. Eshetu, D. Bresser, S. Passerini, *ChemSusChem* **2015**, *8*, 2154.
- [60] I. J. Ong, J. Newman, *J. Electrochem. Soc.* **2019**, *146*, 4360.
- [61] J. Schmalstieg, C. Rahe, M. Ecker, D. U. Sauer, *J. Electrochem. Soc.* **2018**, *165*, A3799.
- [62] S. W. Han, *Ph.D. thesis*, University of Michigan, **2014**.
- [63] M. J. Lain, J. Brandon, E. Kendrick, *Batteries* **2019**, *5*, 1.
- [64] J. B. Quinn, T. Waldmann, K. Richter, M. Kasper, M. Wohlfahrt-Mehrens, *J. Electrochem. Soc.* **2018**, *165*, A3284.
- [65] A. Funabiki, M. Inaba, Z. Ogumi, S. Yuasa, J. Otsuji, A. Tasaka, *J. Electrochem. Soc.* **1998**, *145*, 172.
- [66] J. Marzec, K. Świerczek, J. Przewoźnik, J. Molenda, D. R. Simon, E. M. Kelder, J. Schoonman, *Solid State Ionics* **2002**, *146*, 225.
- [67] D. Carlier, M. Ménétrier, C. Delmas, *J. Mater. Chem.* **2001**, *11*, 594.